

1 **Investigation of processes controlling summertime gaseous elemental mercury**
2 **oxidation at mid-latitude marine, coastal, and inland Sites**

3 **Z. Ye¹, H. Mao¹, C.-J. Lin^{2,3}, and S. Y. Kim⁴**

4 ¹ Department of Chemistry, State University of New York College of Environmental Science and
5 Forestry, Syracuse, NY, 13210, USA

6 ² Center for Advances in Water and Air Quality, Lamar University, Beaumont, TX, 77710, USA

7 ³ Department of Civil and Environmental Engineering, Lamar University, Beaumont, TX, 77710,
8 USA

9 ⁴ R&D Program Evaluation Division Office of National Evaluation and Analysis Korea Institute
10 of S&T Evaluation and Planning (KISTEP), Seoul, South Korea

11 Received: 13 October 2015 – Accepted: 23 October 2015 – Published: 15 January 2016

12 Correspondence to: Z. Ye (zye01@syr.edu)

13

14
15
16
17
18
19
20
21
22
23
24
25
26
27
28
29
30
31
32
33
34
35

Abstract

A box model incorporating a state-of-the-art chemical mechanism for atmospheric mercury (Hg) cycling was developed to investigate oxidation of gaseous elemental mercury (GEM) at three locations in the northeastern United States: Appledore Island (marine), Thompson Farm (coastal, rural), and Pack Monadnock (inland, rural, elevated). The chemical mechanism in this box model included the most up-to-date Hg and halogen chemistry. As a result, the box model was able to simulate reasonably the observed diurnal cycles of gaseous oxidized mercury (GOM) and chemical speciation bearing distinct differences between the three sites. In agreement with observations, simulated GOM diurnal cycles at AI and TF showed significant daytime peaks in the afternoon and nighttime minimums compared to flat GOM diurnal cycles at PM. Moreover, and significant differences in magnitude of GOM diurnal amplitude (AI>TF>PM) were captured in modeled results. At the coastal and inland sites, GEM oxidation was predominated by O₃ and OH, contributing 80–99% of total GOM production during daytime. H₂O₂ initiated GEM oxidation was significant (~33% of the total GOM) at the inland site during nighttime. In the marine boundary layer (MBL) atmosphere, Br and BrO became dominant GEM oxidants with mixing ratios reaching 0.1 and 1 pptv, respectively, contributing ~70% of the total GOM production during mid-day, while O₃ dominated GEM oxidation (50–90% of GOM production) over the remaining day when Br and BrO mixing ratios were diminished. The majority of HgBr produced from GEM+Br was oxidized by NO₂ and HO₂ to form brominated GOM species. Relative humidity and products of the CH₃O₂+BrO reaction possibly affected significantly the mixing ratios of Br or BrO radicals and subsequently GOM formation. Gas-particle partitioning could be potentially important in the production of GOM as well as Br and BrO at the marine site.

36 **1 Introduction**

37 Mercury (Hg) is a toxic pollutant found globally in air, natural waters, and soils. The health
38 concern of Hg arises from the neurotoxic organic form, methyl mercury (MeHg), in the aquatic
39 environments (Mason et al., 2006; Miller et al., 2007; Rolfhus et al., 2003). The high
40 bioaccumulation and biomagnification of MeHg lead to human exposure through the consumption
41 of seafood (Clarkson, 1994). Deposition of atmospheric Hg is one of the most important sources
42 of aquatic Hg.

43 In the atmosphere, Hg exists in three forms: gaseous elemental mercury (GEM), gaseous
44 oxidized mercury (GOM), and particulate bound mercury (PBM). The majority of atmospheric Hg
45 is GEM, comprising > 95% of total gaseous mercury (TGM=GEM+GOM). The 0.8–1.7 years
46 atmospheric lifetime of GEM is conducive to long range transport of Hg as a global pollutant
47 (Bergan et al., 1999; Bergan and Rodhe, 2001; Holmes et al., 2006; Lin and Pehkonen, 1999;
48 Schroeder and Munthe, 1998; Selin et al., 2007). In contrast, GOM and PBM are relatively short-
49 lived and subject to wet deposition and stronger dry deposition than GEM due to their high
50 solubility in water and low vapor pressure. GOM in the atmosphere can be produced from
51 oxidation of GEM, released directly from anthropogenic emissions, and transformed from PBM.
52 In remote regions, in-situ GOM production may be the major source of GOM (Weiss-Penzias et
53 al., 2003; Poissant et al., 2004; Mao and Talbot, 2012) considering its short lifetime.

54 Chemical speciation of atmospheric Hg is essential to understand its geochemical cycle.
55 Theoretical and experimental studies suggested that the main oxidants of GEM in the atmosphere
56 are ozone (O₃), hydroxyl radical (OH), atomic bromine (Br), bromine monoxide (BrO), hydrogen
57 peroxide (H₂O₂), and atomic chlorine (Cl), yielding GOM species of HgO, HgBrO, HgBr,
58 Hg(OH)₂, HgCl, and through further reaction to other mercury halides (Ariya et al., 2015; Dibble

59 et al., 2012; Lin and Pehkonen, 1999). Although efforts have been made to investigate the relative
60 importance of these oxidants for GEM oxidation in the troposphere, it is still not well understood.
61 In the terrestrial environment, it was suggested that the oxidation of GEM was primarily by O₃ and
62 OH radicals (Shon et al., 2005; Sillman et al., 2007). The speciation and quantification of GEM +
63 O₃ product(s) still remain unknown and debatable (Ariya et al., 2015; Gustin et al., 2013; Rutter
64 et al., 2012). An experimental study by Pal and Ariya (2004b) measured 1% of HgO produced by
65 GEM + O₃ on an aerosol filter. Snider et al. (2008) showed HgO(s) production in their kinetic and
66 product study. Schroeder et al. (1998) suggested HgO would not exist as an isolated molecule in
67 gas phase but could be deposited to and retained by manifold given a decomposition temperature
68 of +500 °C. However, the GEM + O₃ reaction and decomposition temperature (Schroeder et al.,
69 1998) could also be impacted by the presence of other ambient gases (Snider et al., 2008; Gustin
70 et al., 2013; Seigneur et al., 1994). A recent study of Huang et al. (2013) observed gas-phase HgO
71 using nylon and cation exchange membranes. The reaction of GEM+OH has been subject to debate
72 between theoretical and experimental studies, as no mechanism consistent with thermochemistry
73 has been proposed (Ariya et al., 2015; Pal and Ariya, 2004a; Subir et al., 2011). Measurement
74 studies on GOM in polar regions (Simpson et al., 2007; Steffen et al., 2008) and sub-tropical MBL
75 (Laurier et al., 2003; Laurier and Mason, 2007; Obrist et al., 2011) as well as atmospheric modeling
76 studies on mercury cycling (Holmes et al., 2009, 2010; Kim et al., 2010; Lindberg et al., 2002;
77 Obrist et al., 2011; Soerensen et al., 2010; Toyota et al., 2014; Wang et al., 2014; Xie et al., 2008)
78 have suggested Br as an important oxidant of GEM. The major source of atmospheric Br was
79 suggested to be produced photolytically from Br-containing compounds and through the Br/BrO
80 cycle involving tropospheric O₃ (Saiz-Lopez and Glasow, 2012; Simpson et al., 2015).

81 GOM concentrations and speciation could be impacted by meteorological conditions and
82 chemical conditions in different environments. High solubility of GOM species, possible phase
83 partitioning of HgO as discussed above could all be the reasons causing varying GOM speciation
84 at different locations. For instance, the aerosol type, size distribution, and chemical composition
85 varied largely between the MBL site and inland sites, which may lead to different gas-particle
86 partitioning rates of GOM species.

87 Hg chemistry in the MBL, the lowest part of the troposphere in direct contact with the sea
88 surface, has global importance as approximately 70% of the earth's surface is covered by oceans
89 (Glasow et al., 2002). Hg in the MBL cycles differently from in coastal or inland areas. However,
90 contemporary models are not able to reproduce GOM observations temporally and spatially due
91 to knowledge gaps in Hg science, simplified model assumptions, and uncertainties of
92 measurements (Ariya et al., 2015; Lin et al., 2006). In the polar region, bromine radicals were
93 identified as the primary cause of the Arctic mercury depletion events (AMDE) (Kim et al., 2010;
94 Lindberg et al., 2002; Toyota et al., 2014; Xie et al., 2008). In the MBL outside Polar Regions,
95 due to lower mixing ratios of atmospheric halogen radicals, often lower than the detection limit,
96 mechanisms for GOM production were more controversial than in Polar Regions. Using a box
97 model, Hedgecock et al. (Hedgecock et al., 2003; Hedgecock and Pirrone, 2004, 2005) suggested
98 that O₃ was a dominant GEM oxidant in the MBL at mid-latitudes in the Mediterranean region,
99 and that the GEM+O₃ reaction may form solid products. However, the reaction kinetics in their
100 model were out-of-date with limited halogen chemistry, and fixed emissions used in the model
101 oversimplified the source terms. Holmes et al. (2009) simulated that GEM oxidation by Br
102 comprised 35–60% of the GOM sources using BrO concentrations calculated at a photostationary
103 state from a prescribed distribution of Br mixing ratios. Additionally, a parameter was introduced

104 in the same study to account for entrainment of free tropospheric GOM into the MBL and the Br
105 mixing ratio was adjusted to capture the observed GOM diurnal trend, which could cause large
106 uncertainties in GOM simulations. Most recently, Wang et al. (2014) employed updated Hg
107 reactions together with bromine and iodine reactions, adopting the free tropospheric GOM
108 entrainment parameter from Holmes et al. (2009) for tropical MBL, and found Br to be a primary
109 GEM oxidant, but oxidation by Br or O₃/OH alone was unable to reproduce observed GOM
110 concentration. However, different GEM oxidants could be dominant in different environments, as
111 a result of the unique composition and concentration levels of in-situ oxidants those environments
112 may be characterized with.

113 In this study, we employed a state-of-the-art chemical mechanism that incorporates gas and
114 aqueous phase chemistry of Hg, O₃, and halogen to investigate the dynamics of GOM formation
115 under various atmospheric conditions in mid-latitude regions. The most up-to-date kinetics was
116 applied. Halogen radical mixing ratios (such as Br and BrO) were calculated using up-to-date
117 atmospheric halogen reactions. Clear sky days with calm wind conditions were selected, which are
118 mostly associated with strong atmospheric stability, to minimize the entrainment effect of free
119 tropospheric air and regional transport and hence no entrainment factor was included in this study.
120 Moreover, the initial GEM mixing ratios along with a list of compounds (Table 2) in the model
121 were obtained from observations in three different environments and were set to be constant during
122 simulations. Fixing the input concentrations of GEM among a number of other compounds (Table
123 2) as constants using observational data enabled a modeled chemical environment close to the real
124 atmospheric environment that is being studied. Moreover, a box model simulates the
125 concentrations of short-lived compounds reaching an instantaneous chemical steady state, and for
126 the time scales of such instants, the chemicals such as GEM are long-lived enough to maintain a

127 constant level. In Section 2, the methods employed were laid out in detail. Section 3 presented
128 results of reasonably simulated differences between GOM diurnal cycles at the three locations that
129 were captured in measurement data, major GEM oxidants in the three environments, and a detailed
130 discussion of the sensitivity of physical parameters and important chemical reactions. Section 4
131 summarized the key findings and implications from this study.

132 **2 Methods**

133 **2.1 Box Model Description**

134 The Kinetic PreProcessor version 2.1 (Sandu and Sander, 2006) was utilized as the
135 framework of the box model (Hedgecock et al., 2003; Hedgecock and Pirrone, 2004, 2005). A
136 second order Rosenbrock method (Verwer et al., 1999) was applied to solve the coupled ordinary
137 differential equations. The box model used in this study was initially set up by Kim et al. (2010).
138 It was further improved in this study by incorporating the most up-to-date gas and aqueous phase
139 chemical mechanisms (Atkinson et al., 2004, 2008; Dibble et al., 2012; Sander et al., 2011) to the
140 model.

141 2.1.1 Reactions and kinetics

142 The box model has a total of 424 reactions: 276 gas-phase reactions (including Hg, halogen,
143 O₃, sulfate, and hydrocarbon reactions), 52 gas-water equilibriums, 28 aqueous equilibriums and
144 68 aqueous reactions. Most of these reactions and kinetic data were updated based on JPL Report
145 No. 17 (Sander et al., 2011), the halogen chemistry reviews of Atkinson et al. (2004, 2008), and
146 the references listed in Table 1. Photodissociation coefficients were calculated from the
147 Tropospheric Ultraviolet and Visible (TUV) Radiation Model (Madronich, 1993).

148 The most important improvements in chemistry are gas and aerosol phase of Hg and
149 halogen reactions. Gas-phase Hg reactions included in the box model are (Table 1):

150 1. Oxidation of GEM by O₃, OH, H₂O₂, Br, BrO, Cl, Cl₂, I (G1–8);
151 2. Reduction of HgBr and HgI to produce GEM (G9–11); and
152 3. Reactions of HgBr/HgCl with BrO, ClO, IO, NO₂, HO₂, and OH (G12–24) with kinetics
153 suggested by Dibble et al. (2012).

154 Aqueous Hg reactions include (Table S1):

155 1. Oxidations of Hg by O₃, OH, HOCl, and ClO⁻, further oxidation of HgOH by O₂;
156 2. Reduction of Hg²⁺ by HO₂, photolytic reduction of Hg(OH)₂ and S(IV)-mediated
157 reduction; and
158 3. Aqueous equilibria involving HgSO₃, Hg(SO₃)₂²⁻, HgOH⁺ and Hg(OH)₂. Gasphase
159 halogen reactions in the box model are mainly cycles of halogen radicals (Cl/Br/I and ClO/BrO/IO
160 radicals).

161 The Cl/Br/I radical cycles include photodissociation of Cl₂/Br₂/I₂, organic halides, and
162 other inorganic halides as sources, and oxidation reactions as sinks. The ClO/BrO/IO radical cycles
163 involve oxidation of Cl/Br/I radicals, photodissociation of ClNO₂/ClONO₂/BrNO₂/BrONO₂,
164 production from other halogen radicals, and sink reactions to calculate Cl/Br/I radicals or other
165 halides. Aqueous halogen reactions include reactions of Br⁻/Cl⁻ and reactions of aqueous BrCl,
166 HCl, HBr, HOCl, HOBr, Cl₂, and Br₂ species. The chemistry of halogen radicals, especially the
167 reaction cycles of Br and BrO radicals, could be important and should not be neglected or replaced
168 by simple approximation. Hence, the most up-to-date halogen chemistry from the literature was
169 included in our model.

170 2.1.2 Initial conditions and input data

171 Observations at three sites from the University of New Hampshire (UNH) AIRMAP
172 Observing Network (<http://www.eos.unh.edu/observatories/data.shtml>) were used: a marine site

173 located on Appledore Island (AI) at the Shoals Marine Lab, the Gulf of Maine (42.97°N, 70.62°W,
174 40 m a.s.l.), a coastal site located in Thompson Farm (TF) in Durham, NH (43.11°N, 70.95°W, 24
175 m a.s.l.) and 25 km away from the Gulf of Maine, and a forested 90 km inland site located on Pack
176 Monadnock (PM) in Miller State Park in Peterborough, NH (42.86°N, 71.88°W, 700 m a.s.l.) (Fig.
177 1). Hourly mean values of GEM, O₃, CO, NO, meteorological observations (i.e., temperature,
178 relative humidity, and solar radiation) at these three sites were used as initial input to the box model.
179 For species that were not measured, we set their initial concentrations as the values in similar
180 environments from the literature if available. Observations of GOM mixing ratios from the three
181 sites were utilized to evaluate the model performance. GEM and GOM data were collected using
182 the Tekran[®] 2537/1130/1135 speciation unit (Tekran Inc., Canada). For these three sites, the
183 instruments were first run and calibrated in the laboratory and then operated at the sites in a
184 consistent manner. GEM was measured at 5-min intervals and with a limit of detection (LOD) of
185 ~5-10 ppqv (Mao et al., 2008), GOM was measured over a 2-h sampling period with a LOD of
186 ~0.1 ppqv based on three times the standard deviation of the field blank values (Sigler et al., 2009;
187 Mao and Talbot, 2012). A custom-built refrigerator assembly and a canister of drierite was used
188 to cool and dry air streams before entering into the 1130 pump module, resulting in < 25% RH of
189 air streams (Sigler et al., 2009). Detailed information on these measurements can be found in Mao
190 and Talbot (2004; 2012), Talbot et al. (2005), Fischer et al. (2007), Mao et al. (2008), and Sigler
191 et al. (2009). Table 2 lists the input variables of the box model. The model's initial mixing ratios
192 of GEM, O₃, CO, and NO were obtained from observations and were set to be constant during
193 each 1h simulation. Br/Cl/I concentrations were all calculated from the model given initial
194 concentrations of 1 pptv (Finley et al., 2008; except for AI) for Br₂, Cl₂, and I₂ species. At AI, the
195 Br₂ initial concentration was set to be constant during simulations and used Saiz-Lopez et al.

196 (2006)'s values to constrain [BrO]. Detailed information can be found in Section 3.3.1. Dry
 197 deposition flux was calculated using dry deposition velocity data derived from Zhang et al. (2009,
 198 2012) and boundary layer height estimated from Mao and Talbot (2004). Other physical
 199 parameters (i.e. Henry's constants, liquid water content, and aerosol radius) were used to simulate
 200 the gas-particle partitioning process in the box model.

201 2.1.3 Gas-particle partitioning

202 An empirical expression was utilized to calculate particle size growth relative to its dry
 203 radius (r_{dry}) (Lewis and Schwartz, 2006):

$$204 \quad r = r_{\text{dry}} \frac{4}{3.7} \left(\frac{2-\text{RH}}{1-\text{RH}} \right)^{1/3}, \quad (1)$$

205 where RH is the relative humidity, and r is the particle radius at RH.

206 Gas-particle partitioning was treated by mass transfer between droplets and air. The
 207 dynamic mass transfer coefficient across the gas-aqueous interface was calculated using the
 208 method developed by Schwartz (1986). The net mass flux (F , molecule $\text{cm}^{-3} \text{s}^{-1}$) between the gas
 209 and aqueous phase is given by

$$210 \quad F = k_{\text{mt}} \times \left(L \times c_{\text{g}} - \frac{c_{\text{aq}}}{\text{HRT}} \right), \quad (2)$$

211 where L is the liquid water content ($\text{m}_{\text{water}}^3 \text{m}_{\text{air}}^{-3}$), k_{mt} is the mass transfer coefficient (s^{-1}), c_{g} is the
 212 gas phase concentration of the species (molecules cm^{-3}), c_{aq} is the aqueous phase concentration of
 213 species (molecules cm^{-3}), H is the Henry's constant of the species (M atm^{-1}), R is the universal gas
 214 constant ($\text{atm L K}^{-1} \text{mol}^{-1}$), and T is atmospheric temperature (K). k_{mt} is calculated as follow:

$$215 \quad k_{\text{mt}} = \left(\frac{r^2}{3D_{\text{g}}} + \frac{4r}{3\bar{v}\alpha} \right)^{-1}, \quad (3)$$

$$216 \quad \bar{v} = (8RT/M\pi)^{1/2}, \quad (4)$$

217 where r is the particle radius (μm), D_g is the diffusion coefficient (m^2s^{-1}), \bar{v} is the mean thermal
218 molecular velocity (m s^{-1}), α is the dimensionless accommodation coefficient, and M is the species
219 molecular weight (g mol^{-1}).

220 **2.2 Case Selection**

221 A total of 83 cases were examined to investigate the role of chemistry in Hg cycling in the
222 MBL, coastal, and inland environments. At the study sites, significant warm season declines of
223 GEM were observed with annual maximums in spring and minimums in autumn resulting in
224 seasonal amplitudes up to 100 ppqv at TF (Mao et al., 2008). The lost GEM during the warm
225 season most likely entered the ecosystem. Chemical transformation of GEM in warm seasons was
226 suspected to be one of the factors causing the observed seasonal decline in GEM. As such, this
227 study selected the cases representing summer days when chemical processes were most likely
228 dominant. To exclude the influence of wet deposition, we selected clear-sky conditions based on
229 the observed photodissociation rate constant of NO_2 ($j\text{NO}_2$) and solar radiation flux. To minimize
230 the influence of transport, cases with arithmetic daily mean wind speed higher than 75% percentile
231 of all summer days in studied years ($> 1.3 \text{ m s}^{-1}$ at TF, $> 6 \text{ m s}^{-1}$ at PM, and $> 7 \text{ m s}^{-1}$ at AI) were
232 excluded. As a result, 50, 12, and 21 clear-sky days at AI (marine), TF (coastal), and PM (inland,
233 elevated), respectively, were selected from summers of 2007, 2008, and 2010. Since there was no
234 temperature data available for summer 2009 at TF, 2009 was not considered.

235 **2.3 Backward Trajectory Model**

236 The National Oceanic and Atmospheric Administration (NOAA) Hybrid Single Particle
237 Lagrangian Integrated Trajectory (HYSPPLIT) trajectory model was used to identify source regions
238 of air masses at the three sites. The model runs were performed over twenty-four hours using the

239 NOAA NAM (Eta) Data Assimilation System (EDAS) data with a 40km×40km horizontal
240 resolution as input. Backward trajectories and trajectory clusters were calculated.

241 **2.4 Model Evaluation**

242 To evaluate the box model performance with observations, the following statistical
243 performance measures (Chang and Hanna, 2004; Hanna, 1988; Hanna et al., 1991, 1993), which
244 include the fractional bias (FB), the normalized mean square error (NMSE), the root mean square
245 error (RMSE), and the partition of NMSE due to systematic errors (NMSE_s) were used:

$$246 \quad FB = (\overline{C_0} - \overline{C_p}) / 0.5(\overline{C_0} + \overline{C_p}), \quad (5)$$

$$247 \quad NMSE = \overline{(C_0 - C_p)^2} / \overline{C_0 C_p}, \quad (6)$$

$$248 \quad RMSE = \sqrt{\overline{(C_0 - C_p)^2}}, \quad (7)$$

$$249 \quad NMSE_s = 4FB^2 / (4 - FB^2), \quad (8)$$

250 where C_p is model predictions, C_0 is observations, overbar ($\overline{}$) is average over the dataset.

251 **3 Results and Discussion**

252 **3.1 General characteristics in measured GOM and GEM**

253 In the selected 83 cases, atmospheric GOM and GEM mixing ratios varied greatly at the
254 three sites (Fig. 2). Mixing ratios of GOM varied over 0.03–87.79 ppqv at AI, 0.04–4.93 ppqv at
255 TF, and 0–0.65 ppqv at PM. At AI and TF, significant diurnal variation was observed with
256 afternoon maximums and nighttime minimums. At AI, GOM peaked at 10 ppqv over 14:00–16:00
257 EDT and was ~ 5 ppqv at night, well above the LOD (~ 0.1 ppqv, from Sigler et al., 2009, the
258 same LOD for the instruments at the three sites). At TF, GOM mixing ratios peaked at 0.75 ppqv
259 at 17:00 EDT and were below LOD at night, before 08:00 EDT. The GOM diurnal cycle at PM
260 was different from that at AI and TF. At PM, averaged GOM had higher mixing ratios at night and

261 in the early morning than in the afternoon. However, the median values showed afternoon peaks
262 and nighttime minimums. The difference between average and median GOM diurnal cycles was
263 driven by 3 cases that had abnormally high GOM mixing ratios (> 0.6 ppqv) at night or in the early
264 morning relative to the average GOM mixing ratio through the day (~ 0.1 ppqv).

265 Mixing ratios of GEM ranged over 65–231 ppqv at AI, 60–213 ppqv at TF, and 121– 231
266 ppqv at PM (Fig. 2). On average, GEM mixing ratios at PM were 8% higher than that at TF and
267 12% higher than that at AI. Unlike GOM, GEM diurnal cycles showed nearly flat patterns at AI
268 and PM, though slightly higher (~ 3 %) GEM mixing ratios at night than in the daytime were
269 observed at PM. In contrast, the average GEM diurnal cycle at TF showed an early morning (07:00
270 EDT) minimum (112 ppqv) and a daytime (13:00 EDT) maximum (153 ppqv).

271 The site differences of GOM and GEM diurnal cycles could be attributed to different
272 chemical environments, land surface types, and meteorological conditions. For example, the GEM
273 daily minimum at night and in the early morning at TF was likely caused by a strong net loss
274 dominated by dry deposition under nocturnal inversion (Mao et al., 2008; Mao and Talbot, 2012).
275 Nocturnal inversion also influenced the GEM and GOM diurnal cycles at PM, albeit differently
276 from at TF. The elevation of PM site is 700ma.s.l., above the nocturnal inversion layer (< 200 m)
277 (e.g. Kutsher et al., 2012), and thus GEM and GOM at night were continuously replenished by
278 those produced from daytime and remaining in the residual layer, which likely caused higher
279 nighttime values at PM. Daytime peaks of GOM at TF and AI were most likely caused by
280 photochemical oxidation of GEM under strong solar radiation. The causes for such variation were
281 examined in Sect. 3.4.2.

282 3.2 Simulated diurnal variation and speciation of GOM

283 Model simulated diurnal cycles of GOM averaged over the 50, 12, and 21 clear-sky days
284 at AI, TF, and PM, respectively, were shown in Fig. 2. The patterns of diurnal variation were
285 similar at the three sites with small discrepancy on the occurring time of daily peaks (~ 13:00 LT
286 at AI, and ~14:00 LT at TF and PM), but the magnitude varied large by site. AI had the largest
287 GOM diurnal amplitude (i.e., daily maximum – daily minimum) ranging from 0.73 to 13.29 ppqv,
288 TF from 0.05 to 0.57 ppqv, and PM showed a very small range from 0.05 to 0.14 ppqv. Similar
289 magnitude variation was also exhibited in GOM observations (Fig. 2). Overall, simulated GOM
290 mixing ratios at the three sites were in agreement with observations (detailed comparison in Sect.
291 3.3).

292 The simulations suggested that the dominant GOM species and GEM oxidants varied by
293 site (Fig. 3). At AI, brominated GOM species comprised 59–81% of the total GOM over 08:00–
294 18:00 EDT, whereas HgO was dominant (50–92% of the total GOM) during the remaining day.
295 At TF and PM, HgO was the predominant GOM species (62–88%). HgO was produced from
296 oxidation of GEM by O₃ and OH. The contribution to HgO from oxidation by O₃ was larger than
297 by OH except at noon when OH mixing ratios reach daily peaks resulting in comparable
298 contributions (48 and 52% by OH and O₃, respectively). At AI, BrHgNO₂ and HgBrO were the
299 most abundant brominated GOM species, which constituted ~ 96% of the total brominated GOM.
300 HgBrO was produced from the GEM + BrO reaction, while BrHgNO₂ were produced from GEM
301 oxidation by Br radicals followed by reactions of HgBr with NO₂. Hg(OH)₂ from GEM oxidation
302 by H₂O₂ appeared to be an important nighttime GOM species at the inland site (PM), accounting
303 for 33% of the total GOM at night. Other GOM species were negligible in the studied cases.

304 3.3 Model evaluation

305 For all cases at AI and TF, the average simulated and observed GOM diurnal cycles agreed
306 reasonably well in both magnitude and shape, whereas at PM the model appeared to have missed
307 both (Fig. 2). Three salient features were noted for the disagreement between the model and
308 observational results. First, the standard deviation of observed GOM mixing ratios was a factor of
309 2–7 larger than that of the simulated. This suggested that the model could capture the mean values
310 of GOM, but not the very low and very large mixing ratios. Second, observed nighttime GOM
311 mixing ratios were 12–200% larger than the simulated at AI, indicating that the model did not
312 capture certain nighttime processes producing GOM in the MBL. Third, the simulated diurnal
313 cycle was the opposite of the observed at PM, with the maximum during the day and minimum at
314 night. It was likely that the model simply simulated the dependence of GOM production on solar
315 radiation. At PM, more processes may have contributed to the diurnal variation. At night, the site
316 is above the nocturnal boundary layer and exposed to the GOM produced in the preceding
317 convective boundary layer, which could continually replenish surface GOM at the site that was
318 lost via dry deposition and perhaps reduction. The model-observation discrepancies of GOM at
319 the three sites were discussed as follows.

320 3.3.1 Appledore Island (marine)

321 Of the 50 cases at AI, 27 diurnal cycles of GOM were simulated with the average values
322 and patterns close to the observed and $NMSE_s = 1.88\%$, denoted as *matching* cases hereafter, 8
323 were underestimated with $NMSE_s = 121\%$, and 15 were overestimated with $NMSE_s = 171\%$. The
324 observed and simulated average GOM mixing ratios and the corresponding ranges were calculated
325 for the matching, under-estimation, and over-estimation cases at AI (Fig. 4a). For more than half
326 of the time (27 matching cases out of 50 cases in total), the model captured the average GOM

327 diurnal cycle, the diurnal cycle pattern and overall GOM levels. Beyond that, Fig. 4a shows large
328 difference in the observed GOM levels among the matching, under-estimation, and over-
329 estimation cases. On average, the observed daytime peak in the under-estimation cases was about
330 twice as large as that for the matching cases and 7 times larger than that for the over-estimation
331 cases. However, such difference was not captured by the model, suggesting that some GOM
332 producing processes in the MBL were not included or not realistically represented in the box model.
333 In addition, the GOM diurnal pattern in the over-estimation cases was different from those in the
334 under-estimation and matching cases. The average observed GOM diurnal cycles of the under-
335 estimation and matching cases both exhibited a daily maximum at 13:00 EDT and a minimum over
336 04:00–08:00 EDT, whereas the over-estimation cases showed a daily maximum at around 20:00
337 EDT and a minimum at 07:00–08:00EDT.

338 Such differences were due possibly to the challenges of simulating Br and BrO in the MBL
339 at AI. No measurements of Br and BrO radicals as well as Br₂ were available at AI. To reasonably
340 simulate mixing ratios of Br and BrO, Br₂ mixing ratios were calculated based on the BrO
341 observations at a mid-latitude MBL site from Saiz-Lopez et al. (2006), which was ~5.6 ppqv during
342 the daytime (06:00–21:00 EDT). Saiz-Lopez et al. (2006) showed that daytime peak mixing ratios
343 of BrO in the MBL could vary by a factor of 2 over a time period of 3 days. Such variation was
344 not captured in our box model, potentially resulting in uncertainty of up to 100% in simulated Br
345 mixing ratios with subsequent effects on GOM simulation.

346 In the over-estimation cases, the simulated GOM daytime peaks were very low and
347 appeared later during the day than in the under-estimation and matching cases. Considering the
348 late afternoon peak (17:00 EDT) of O₃ compared to the noontime peak of Br radicals, O₃ possibly
349 played a more important role in the over-estimation cases. To verify this hypothesis, a sensitivity

350 simulation was conducted without the initial Br₂ mixing ratio fixed for these cases, termed as the
351 O₃/OH scenario. In this sensitivity runs, the Br₂ concentration rapidly diminished with time leading
352 to very low concentrations of Br and BrO. The O₃/OH scenario turned out to better represent these
353 15 overestimation cases with NMSE_s = 34% (compared to 167% with Br₂ mixing ratio fixed).

354 These sensitivity simulations suggested that in the MBL, Br may be a dominant GEM
355 oxidation most of the time, but at times of low Br mixing ratios, O₃ could become dominant. To
356 identify the origin of the air masses at AI, backward trajectory analysis was conducted using the
357 HYSPLIT4 model (<https://ready.arl.noaa.gov/HYSPLIT.php>). All 24 h backward trajectories
358 started from the time of GOM daily peaks for the 50 cases. The trajectory results were clustered
359 for over-estimation, matching, and under-estimation cases (Fig. 5). Based on these trajectories, in
360 about half of the 15 over-estimation cases air masses originated from marine environments, while
361 in more than 80% of the 27 matching cases and 7 out of 8 under-estimation cases air masses came
362 from inland northwest of AI. Note that in those under-estimation cases GOM mixing ratios were
363 exceptionally large, exceeding 30 ppqv.

364 Different source areas of air masses reaching AI could be one of the reasons for the large
365 variation of GOM observations. The highest levels of GOM were observed in summer with RH
366 roughly < 50% at AI (Mao et al., 2012). A close examination of the 50 cases at AI revealed low
367 RH levels ($\leq 45\%$) on 16 days. The time periods with RH $\leq 45\%$ appeared mostly (78% of the
368 time) in the afternoon over 12:00–20:00 EDT and less so (22%) at night over 21:00–02:00 EDT.
369 During these time periods, increased GOM (15 out of 16, compared with periods with high RH on
370 the same day) and daily maximum GOM (10 out of 16) occurred simultaneously at low RH,
371 regardless of the time of the day.

372 Interestingly, the RH level of 45% corresponds to the crystallization point of NaCl (Cziczo

373 et al., 1997; Tang et al., 1997). The crystallization of sea-salt aerosols might be link to the very
374 high GOM peaks in certain ways. Rutter and Schauer (2007) found that particles of potassium and
375 sodium chlorides had high partitioning coefficients that could shift the GOM gas-particle
376 partitioning toward the aqueous phase, while ammonium sulfate, levoglucosan, and adipic acid
377 would shift the partitioning toward the gas phase. It was thus *hypothesized* that, when these inland
378 air masses reached the MBL mixed with the marine air, the processes discussed above might have
379 been activated involving the interaction between land and marine air, which potentially resulted in
380 those very high GOM mixing ratios.

381 Laskin et al. (2012) found effective reactivity of chloride (Cl^-) components with organic
382 acid in sea salt aerosols (SSAs), possibly leading to depletion of Cl^- and formation of organic salts
383 in aerosols. Biogenic compounds in air masses originating from inland forested areas could be
384 oxidized forming organic acids in transit. As inland air reached the MBL, these organic acids
385 would deposit onto SSAs and could subsequently change SSAs' chemical and physical properties,
386 such as lowering concentrations of Cl^- and forming a thick organic film on the outside of SSAs.
387 The lower concentrations of Cl^- and higher concentrations of organic acid in aerosols might have
388 contributed to the shift in the gas-to-particle partitioning to the gas phase and resulted in higher
389 GOM mixing ratios in the atmosphere.

390 Another possible explanation could be air masses of inland origin encountering marine air
391 rich in atmospheric Br and BrO radicals. The main source of atmospheric Br is thought to come
392 from the release of Br_2 and BrCl from SSA (Finlayson-Pitts, 2010; Sander et al., 2003).
393 Experimental studies suggested Br^- enhancements of a factor of 40 to 140 on the surface of
394 sufficiently dry artificial SSA (Ghosal et al., 2008; Hess et al., 2007). Therefore, when drier inland
395 air masses were mixed with marine air in the MBL under relatively low RH conditions, SSA

396 became drier, forcing more Br₂ to be released from SSA, resulting in enhanced oxidation of GEM
397 by Br and BrO radicals. These hypotheses need to be validated in future research. These
398 mechanisms are presently missing in the box model, leading to the model's inability to capture
399 very high GOM mixing ratios. Measurements of halogen species and a better gas-particle
400 partitioning mechanism are needed to better the model's performance.

401 3.3.2 Thompson Farm (coastal)

402 Generally, the box model performed well at TF (Fig. 2) with overall NMSE_s = 0.75% and
403 RMSE = 0.78 ppqv. Of the 12 cases at TF, 6 diurnal cycles of GOM (50%) were simulated
404 reasonably well with NMSE_s < 50 %, 2 were underestimated by ~ 70 %, and 4 cases were
405 overestimated by a factor of 2 to 5. Overall, the observed average diurnal cycles of GOM for all
406 selected summer clear-sky days at TF had daily peaks during 14:00–20:00 EDT with very low
407 values at night between 0:00 and 8:00 EDT (Sigler et al., 2009) (Fig. 2). The peak observed at
408 17:00 EDT (Fig. 2) was largely affected by the abnormally high GOM peak in that one under-
409 estimation case (Fig. 4b).

410 For the over-estimation and matching cases, the model reproduced very low GOM mixing
411 ratios at night (Fig. 4b). For the same reason substantially lowering GEM mixing ratios at night
412 and in the early morning at TF (Mao et al., 2008), the low nighttime GOM at TF was probably
413 caused by loss via dry deposition under nocturnal inversion. To capture these low values in model
414 simulations, realistic nocturnal boundary layer height data were needed beside solid representation
415 of dry deposition and chemistry in the model. The diurnal cycle of boundary layer height in the
416 box model was parameterized based on reanalysis data obtained from the Research Data Archive
417 at the National Center for Atmospheric Research (<http://rda.ucar.edu/datasets/ds093.0/>). Use of
418 these data helped to reproduce the low nighttime GOM levels in simulations for the TF site.

419 Another notable feature in Fig. 4b is the exceedingly high observed GOM mixing ratios in the
420 under-estimation cases and the low observed GOM mixing ratios throughout the day in all over-
421 estimation cases. Observed GOM mixing ratios in the under-estimation cases showed a factor of
422 3–4 larger than those in the matching cases, and a factor of 3–31 larger than those in the over-
423 estimation cases (Fig. 4b). Concurrently, larger fine particle concentrations, 7468 cm^{-3} on average,
424 were observed for the under-estimation cases, which was 51 and 80% larger than those in the
425 matching cases and over-estimation cases, respectively. Lower RH, 66% on average, was observed
426 in the under-estimation cases, 5 and 11% lower than that in the matching and over-estimation cases,
427 respectively. Moreover, higher air pressure (1018, 8 and 12 hPa larger than the matching and over-
428 estimation cases, respectively), lower wind speed (0.8 m s^{-1} on average, 35 and 68% lower than
429 matching and over-estimation cases respectively), and stronger solar radiation flux (8 and 13%
430 stronger than matching and over-estimation cases respectively) were found in the under-estimation
431 cases. An examination of the sea level pressure maps (Figure S1) in the under-estimation cases
432 suggested that these cases occurred under the strongest Bermuda High influence, with the calmest,
433 sunniest, and driest conditions of all cases, which is most conducive to photochemistry and
434 pollution build-up that may have ultimately contributed to the very large GOM mixing ratios in
435 those under-estimation cases. Our model appeared to fail to mimic the chemistry under such
436 conditions that produced the largest GOM mixing ratios.

437 3.3.3 Pack Monadnock (inland, rural, elevated site)

438 At PM, diurnal cycles of GOM were overestimated with $\text{NMSE}_s = 70\%$ and overall
439 $\text{RMSE} = 0.13 \text{ ppqv}$. However, considering the extremely low mixing ratios of GOM observed at
440 PM (Fig. 2), cases with $\text{RMSE} < 0.1 \text{ ppqv}$ (LOD) were considered as matching cases. Therefore,
441 the model reasonably simulated 11 out of 21 (52%) cases, underestimated in 1, and overestimated

442 in 9. Evaluation of simulated GOM diurnal cycles against observations (Fig. 2) showed reasonable
443 agreement with general overestimation ranging over 0.05–0.07 ppqv.

444 The observed GOM diurnal cycle (Fig. 2f) showed daily maximums at 08:00 and 23:00
445 EDT, which were mainly influenced by the underestimated case (Fig. 4c). In comparison, the
446 remaining (95 %) cases showed a very flat GOM diurnal cycle at PM. The first and most important
447 reason for such observation-model discrepancy is that the PM site is a mountain site (700 m a.s.l.),
448 which is above the nocturnal inversion layer (~200m at TF) but within the convective boundary
449 layer during the day. At night, a regional pool of GOM produced in the preceding convective
450 boundary layer remained in the residual layer, which kept the surface GOM levels from dropping
451 below the LOD at night at PM. The slight decline of GOM mixing ratios after sunrise was because
452 of mixing with the lower altitude air masses with depleted GOM from the night. The effect of the
453 PM's site characteristics was not represented in the box model, which could result in model's
454 inability to simulate diurnal variation associated with this aspect of the site. In addition, due to the
455 dominance of GEM oxidation by O₃ in GOM production in the model, it was highly likely that the
456 flat diurnal cycles (slightly higher at night) of GEM (Fig. 2) and O₃ were mirrored in GOM mixing
457 ratios.

458

459 **3.4 Sensitivity analysis**

460 3.4.1 Sensitivity of GOM to physical and chemical parameters

461 The base scenario (*Scenario 0*) of these sensitivity runs represented the real atmospheric
462 conditions on the selected 50 days at AI. *Scenarios 1–10* are sensitivity runs where one parameter
463 in the base scenario was changed at the time (Table 3). *Scenario 1* turned off photolysis reactions.
464 *Scenarios 2–4* tested the gas-particle partitioning scheme. The liquid water content range was

465 derived from Hedgecock et al. (2003). *Scenarios 5–9* tested the sensitivity of GOM mixing ratios
466 to GEM oxidation reactions and their coefficients. *Scenarios 10–11* tested the sensitivity of GOM
467 mixing ratios to temperature. The temperature range was based on the observed average
468 temperature diurnal cycle.

469 The importance of photochemical radicals in GEM oxidation was demonstrated clearly in
470 decreases of 3-92 and 2-100 % in daytime GOM and PBM, respectively with largest decreases at
471 noon as a result of turning off photochemistry (*Scenario 1*). *Scenario 2* showed ~74% of oxidized
472 Hg transformed to PBM at AI with gas-particle partitioning switched on. In this scenario, HgO
473 and Hg(OH)₂ were more sensitive than halogenated GOM species (such as BrHgNO₂). Turning
474 off gas-particle partitioning more than quadrupled the mixing ratios of HgO and Hg(OH)₂
475 throughout the day compared to increases of more than 100 and 60% halogenated GOM species
476 during daytime and nighttime, respectively.

477 Decreasing liquid water content by 1 order of magnitude tripled GOM mixing ratios,
478 whereas increasing the same amount decreased GOM by 80% (*Scenarios 3–4*). Sensitivity of
479 GOM and PBM mixing ratios to dominant GEM oxidation reactions are shown in *Scenarios 5–9*.
480 Using the slowest rate coefficient of GEM + O₃ obtained from Hall (1995), as opposed to the one
481 from Snider et al. (2008) led to a decrease of 56.7% in HgO, and decreases of 15 and 85% in total
482 GOM during daytime and nighttime, respectively. Using an order of magnitude faster rate
483 coefficient of GEM + Br from Ariya et al. (2002) increased 250% of total GOM during daytime.
484 Turning off GEM oxidation by O₃, OH, or Br resulted in decreases of 16, 10, and 48%, respectively,
485 in daytime GOM mixing ratios. Turning off the GEM + Br oxidation reaction also decreased
486 daytime PBM mixing ratios by 60%. However, for nighttime GOM and PBM mixing ratios,

487 turning off the GEM + O₃ reaction caused decreases of 88 and 51%, respectively, since Br and OH
488 are both photochemical radicals and O₃ was the predominant oxidant for GEM in the model.

489 *Scenarios 10–11* suggested that nighttime GOM and PBM mixing ratios were more
490 sensitive to temperature than those during daytime. Increasing temperature by 10 K caused a 9%
491 increase each in GOM and PBM mixing ratios during daytime but a decrease of 13% in GOM and
492 54% in PBM at night. This was because the rate coefficient of GEM + O₃ increases with increasing
493 temperature, but the rate coefficient of GEM + OH decreases with increasing temperature.

494 In summary, the parameters used in gas-particle partitioning process, including solar
495 radiation values, temperature, and the rate coefficients of major GEM oxidation reaction, could all
496 affect the GOM simulation but with varying degree. Aerosol properties were suggested to play a
497 very important role in the partitioning of ambient GOM and PBM species and thus should be better
498 represented in future Hg model simulation studies. Using a slower rate coefficient of GEM + O₃
499 (Hall, 1995) had similar effects as not including the GEM + O₃ reaction, i.e. decreasing GOM
500 mixing ratios, especially at nighttime, and brominated GOM species becoming dominant. The
501 GEM + OH reaction was not as important as GEM + O₃ or Br. The use of a higher GEM + Br rate
502 coefficient derived from the study by Ariya et al. (2002) caused more than a factor of 3 higher
503 GOM and PBM resulting in overestimated GOM for most cases. GOM and PBM production
504 appeared to favor lower temperature at daytime and higher temperature at night, and simulated
505 GOM concentrations were not as sensitive to temperature change as to solar radiation and gas-
506 particle partitioning.

507 3.4.2 Influence of physical and chemical processes on GOM diurnal cycle

508 Large variations were exhibited in both observed and simulated GOM mixing ratios at AI,
509 TF, and PM (Fig. 2). Considering that all cases were under relatively calm, clear-sky conditions,

510 the simulated GOM mixing ratio and diurnal cycle were controlled primarily by chemical reactions,
511 dry deposition, and gas-particle partitioning. To quantify the contribution of processes to the
512 difference of GOM mixing ratios at the three sites, two sensitivity scenarios were conducted: use
513 the same physical parameters as those of AI for TF (denoted as TF_AIaerodry) and PM (denoted
514 as PM_AIaerodry).

515 Comparison of simulated GOM diurnal cycles from the AI, TF_AIaerodry and
516 PM_AIaerodry scenarios showed the influence of different chemical scenarios on GOM mixing
517 ratios at the three sites. At night, GOM mixing ratios at the three sites did not vary significantly
518 (0-2 ppqv), with higher values at PM than those at AI and TF (Fig. 6). However, the mid-day peak
519 at AI was more than a factor of two greater than those in the PM_AIaerodry and TF_AIaerodry
520 scenarios, indicating more chemical transformation of Hg occurring at AI. The daytime mixing
521 ratios of GOM at TF and PM were similar, while the nighttime GOM mixing ratios at PM were
522 30-52% higher than at AI and 20-200% higher than at TF. This probably resulted from larger
523 nighttime GEM and O₃ mixing ratios, hence producing more GOM, at PM than at TF and AI.
524 Specifically, nighttime GEM mixing ratios at PM were 8-15% higher than at AI and 8-34% higher
525 than TF cases, while nighttime O₃ mixing ratios at PM were 11-70% larger than at AI and 35-260%
526 larger than at TF. PM had higher nighttime GEM and O₃ mixing ratios, because this site was
527 exposed in the residual boundary layer at night due to its high elevation, constantly replenished
528 with the regional pool of air from the preceding convective boundary layer. Overall, chemical
529 transformation contributed ~60% of the daytime difference in GOM between AI and the two sites
530 over land (TF and PM), 33% of the nighttime difference between AI and TF, and 26% of the
531 difference between PM and AI.

532 In summary, the sensitivity scenarios suggested that dry deposition and gas-particle
533 partitioning contributed 4-37% and 30-96%, respectively, of the total GOM difference between AI
534 and PM. Both processes had larger contributions at night than during daytime. Dry deposition
535 contributed 6-24% of the GOM difference between AI and TF and gas-particle partitioning 18-
536 78%.

537 3.4.3 Br chemistry in the MBL

538 Diurnal cycles of Br and BrO radicals (Fig. 7) were simulated using the Br chemical
539 mechanism described in Sect. 2. Photodissociation of Br₂ was the main source of Br and BrO
540 radicals during daytime. Our simulations suggested that reactive Br compounds were significant
541 gaseous oxidants of GEM in the MBL at a fixed initial mixing ratio of 5.6 ppqv for Br₂. Increasing
542 initial mixing ratios of Br₂ by 25% resulted in an increase of 0.01–2.15 ppqv in GOM mixing ratios.

543 In addition, the reaction of BrO with methyldioxy (CH₃O₂) radicals could have important
544 influence on the mixing ratios of Br, BrO, and GOM. Simulated daytime mixing ratios of CH₃O₂
545 was ~ 40 pptv, and the rate coefficient of $(5.7 \pm 0.6) \times 10^{-12} \text{ cm}^3 \text{ molecule}^{-1} \text{ s}^{-1}$ at 298 K for BrO +
546 CH₃O₂ (Aranda et al., 1997) was used for our simulations. Pathways B1, B2, and B3 were
547 suggested by Aranda et al. (1997) based on an experimental study (Table 4). However, the
548 production of CH₃O may be due to its self-reaction in B1. Guha and Francisco (2003) suggested
549 CH₃OOOBr to be a likely intermediate of this reaction, and that CH₃OOOBr could dissociate to
550 CH₂O+HOObBr (B4, Table 4). Based on thermodynamics calculations, CH₃OBr and O₂ (B3, Table
551 4) were possible products. BrOO and HOBr were both included in the Br chemical cycle and can
552 be transformed back to Br and BrO radicals in the model. However, it is unclear whether CH₃OBr
553 (product of B3) or HOObBr (product of B4) could be transformed back to Br and BrO radicals in

554 the atmosphere. In this case, using the B3 or B4 pathway did not appear to make a difference in
555 our box model results.

556 In this study, the B1 and B2 pathways were used for the $\text{CH}_3\text{O}_2 + \text{BrO}$ reaction as part of
557 the base scenario (denoted as Sim-avg BrOO). The sensitivity run Sim-avg CH_3OBr used the B3
558 pathway in lieu of B1 and B2. The simulated average and the range of GOM diurnal cycles in the
559 base and sensitivity scenarios were evaluated against observed mean and median GOM diurnal
560 cycles of the 50 study cases at AI (Fig. 8). If the $\text{CH}_3\text{O}_2 + \text{BrO}$ reaction followed the B1 and B2
561 pathways, this reaction had a negligible effect on reactive Br radicals. However, if B3 or B4 was
562 applied, the simulated total GOM mixing ratio was lowered by 50% during daytime. Moreover,
563 the simulated GOM diurnal cycle in the base scenario agreed favorably with the observed average
564 GOM diurnal cycle (NMSE= 15 %), while the results of the Sim-avg CH_3OBr scenario were in
565 better agreement with the observed median GOM diurnal cycle (NMSE= 14%). These agreements
566 indicated that, if the $\text{BrO} + \text{CH}_3\text{O}_2$ reaction was a net sink of BrO radicals, the model was able to
567 simulate most cases better, whereas if the product of $\text{BrO} + \text{CH}_3\text{O}_2$ was transformed back to Br or
568 BrO radicals, the model appeared to capture those cases with large GOM mixing ratios (> 6 ppqv).
569 Due to the scarcity of kinetic research on the B3 and B4 pathways, we used B1 and B2 pathways
570 for $\text{CH}_3\text{O}_2 + \text{BrO}$ reaction in this study.

571 In short, the pathways of $\text{BrO} + \text{CH}_3\text{O}_2$ could play an important role in atmospheric Br
572 chemistry and Hg speciation in Br-rich environments. Research on the reaction pathways and rate
573 coefficients of the $\text{BrO} + \text{CH}_3\text{O}_2$ reaction is warranted to better assess the role of this reaction.

574 **4 Summary**

575 This study provided a state-of-the-art chemical mechanism with most up-to-date Hg and
576 halogen chemistry and tested the mechanism for three different environments using a mercury box

577 model. Eighty-three summer clear-sky days were selected at marine, coastal, and inland elevated
578 sites in southern New Hampshire to evaluate the model. As a result, for each of the three
579 environments, GOM diurnal cycles of over half selected cases were reasonably represented by the
580 box model. It was hypothesized, based on the key results and discussion presented in Section 3,
581 that dry air masses with organic compounds transported from inland may result in very large GOM
582 mixing ratios in the MBL possibly due to changing physical and chemical properties of sea salt
583 aerosols. The low nighttime and morning GOM mixing ratios at coastal site were likely a result of
584 a net loss due to dry deposition in the nocturnal inversion layer. The GOM mixing ratios above the
585 LOD at the inland site at night were probably caused by constant replenishment from a regional
586 pool, in the residual boundary layer, of GOM that was produced in the preceding daytime
587 convective boundary layer. The updated chemical mechanism largely improved the simulation of
588 the magnitude and pattern of GOM diurnal variation at the coastal and inland sites. HgO produced
589 from oxidation of GEM by O₃ and OH dominated GOM species at the coastal and inland sites,
590 while bromine-induced mercury species (mainly BrHgOOH, BrHgOBr, and HgBrO) were
591 important at the marine site. In Br chemistry, the products of the CH₃O₂ + BrO reaction strongly
592 influenced the simulated Br and Hg concentrations. In this study, GEM oxidation by O₃ and OH
593 was represented in ways similar to those in regional and global models, which is limited by the
594 current nebulous understanding of potential surface chemistry.

595 It should be noted that without measurements of speciated GOM, modeling results cannot
596 be used to conclusively identify the dominant oxidants of Hg, as well as dominant GOM species
597 in that matter, in the atmosphere. Indeed, the potential uncertainty in ambient Hg measurements
598 especially GOM is a major concern in the community. That being said, it is unlikely to have a
599 quantitative understanding of the bias of our GOM concentrations. Recent laboratory experiments

600 and reviews (Lyman et al., 2010; Jaffe et al., 2014; McClure et al., 2014; Huang and Gustin, 2015;
601 Gustin et al., 2015) reported O₃ and relative humidity (RH) interferences on mercury halides for
602 KCl-coated denuder, the part of Tekran 1130 unit commonly used for GOM field measurements.
603 As stated in Section 2, in our GOM measurement the RH effect was minimized by adding
604 refrigeration to remove excess of water in the airstream. O₃ interference and bias low GOM
605 collection efficiency of KCl-coated denuders were limited to a handful of GOM species in
606 laboratory experiments and remain untested in field measurements. If the measured GOM
607 concentrations were indeed biased low by a factor of 2 or 3 under certain conditions as previous
608 studies speculated, the matching cases at AI and TF would be reduced from 50% of the total cases
609 to 30%, and the model would potentially underestimate GOM concentrations in the remaining
610 cases (70%) by a factor of 3 to 4. It is however hard to speculate the effect at PM since most GOM
611 observations there were below the LOD. This suggested even greater unknowns in our
612 understanding of Hg chemistry. Therefore, more experimental or theoretical studies on Hg
613 reactions and better GOM measurement data are warranted to improve our understanding and
614 subsequently model simulations of atmospheric Hg cycling, which can ultimately serve policy-
615 making in an effective manner.

616 **Acknowledgements**

617 This work is funded by NSF AGS grant # 1141713. We thank T. Dibble, Y. Zhou, Y. Zhang, and
618 C. B. Hall for valuable suggestions and help. We are grateful to the three anonymous reviewers
619 for their thoughtful, detailed, constructive comments, which helped to improve the clarity of the
620 paper.

621

622 References

- 623 Aranda, A., Le Bras, G., La Verdet, G., and Poulet, G.: The BrO + CH₃O₂ reaction: kinetics and
624 role in the atmospheric ozone budget, *Geophys. Res. Lett.*, 24, 2745–2748, 1997.
- 625 Ariya, P. A., Khalizov, A., and Gidas, A.: Reactions of gaseous mercury with atomic and molecular
626 halogens: kinetics, product studies, and atmospheric implications, *J. Phys. Chem. A*, 106, 7310–
627 7320, 2002.
- 628 Ariya, P. A., Amyot, M., Dastoor, A., Deeds, D., Feinberg, A., Kos, G., Poulain, A., Ryjkov, A.,
629 Semeniuk, K., Subir, M., and Toyota, K.: Mercury physicochemical and biogeochemical
630 transformation in the atmosphere and at atmospheric interfaces: a review and future directions,
631 *Chem. Rev.*, 115, 3760–3802, doi:10.1021/cr500667e, 2015.
- 632 Atkinson, R., Baulch, D. L., Cox, R. A., Crowley, J. N., Hampson, R. F., Hynes, R. G., Jenkin, M.
633 E., Rossi, M. J., and Troe, J.: Evaluated kinetic and photochemical data for atmospheric chemistry:
634 Volume I – gas phase reactions of Ox, HOx, NOx and SOx species, *Atmos. Chem. Phys.*, 4, 1461–
635 1738, doi:10.5194/acp-4-1461-2004, 2004.
- 636 Atkinson, R., Baulch, D. L., Cox, R. A., Crowley, J. N., Hampson, R. F., Hynes, R. G., Jenkin, M.
637 E., Rossi, M. J., Troe, J., and Wallington, T. J.: Evaluated kinetic and photochemical data for
638 atmospheric chemistry: Volume IV – gas phase reactions of organic halogen species, *Atmos. Chem.*
639 *Phys.*, 8, 4141–4496, doi:10.5194/acp-8-4141-2008, 2008.
- 640 Balabanov, N. B., Shepler, B. C., and Peterson, K. A.: Accurate global potential energy surface
641 and reaction dynamics for the ground state of HgBr₂, *J. Phys. Chem. A*, 109, 8765–8773, 2005.
- 642 Baumgardner, D., Raga, G. B., Kok, G., Ogren, J., Rosas, I., Báez, A., and Novakov, T.: On the
643 evolution of aerosol properties at a mountain site above Mexico City, *J. Geophys. Res. -Atmos.*,
644 105, 22243–22253, doi: 10.1029/2000JD900299, 2000.
- 645 Bergan, T. and Rodhe, H.: Oxidation of elemental mercury in the atmosphere; constraints imposed
646 by global scale modelling, *J. Atmos. Chem.*, 40, 191–212, 2001.
- 647 Bergan, T., Gallardo, L., and Rodhe, H.: Mercury in the global troposphere: a three-dimensional
648 model study, *Atmos. Environ.*, 33, 1575–1585, 1999.
- 649 Chang, J. C. and Hanna, S. R.: Air quality model performance evaluation, *Meteorol. Atmos. Phys.*,
650 87, 167–196, doi: 10.1007/s00703-003-0070-7, 2004.
- 651 Clarkson, T. W.: The toxicity of mercury and its compounds, in: *Mercury Pollution: Integration*
652 *and Synthesis*, edited by: Watras, C. J. and Huckabee, J.W., Boca Raton, FL, USA, 631–641, 1994.
- 653 Cziczo, D. J., Nowak, J. B., Hu, J. H., and Abbatt, J. P. D.: Infrared spectroscopy of model
654 tropospheric aerosols as a function of relative humidity: observation of deliquescence and
655 crystallization, *J. Geophys. Res.-Atmos.*, 102, 18843–18850, 1997.

656 Dibble, T. S., Zelic, M. J., and Mao, H.: Thermodynamics of reactions of ClHg and BrHg radicals
657 with atmospherically abundant free radicals, *Atmos. Chem. Phys.*, 12, 10271–10279,
658 doi:10.5194/acp-12-10271-2012, 2012.

659 Donohoue, D. L., Bauer, D., and Hynes, A. J.: Temperature and pressure dependent rate
660 coefficients for the reaction of Hg with Cl and the reaction of Cl with Cl: a pulsed laser
661 photolysis/pulsed laser induced fluorescence Study, *J. Phys. Chem. A*, 109, 7732–7741, 2005.

662 Finlayson-Pitts, B. J.: Halogens in the troposphere, *Anal. Chem.*, 82, 770–776, doi:
663 10.1021/ac901478p, 2010.

664 Finley, B. D. and Saltzman, E. S.: Observations of Cl₂, Br₂, and I₂ in coastal marine air, *J. Geophys.*
665 *Res.*, 113(D21), D21301, doi:10.1029/2008JD010269, 2008.

666 Fischer, E. V., Ziemba, L. D., Talbot, R.W., Dibb, J. E., Griffin, R. J., Husain, L., and Grant, A.
667 N.: Aerosol major ion record at Mount Washington, *J. Geophys. Res.-Atmos.*, 112, D02303, doi:
668 10.1029/2006JD007253, 2007.

669 Ghosal, S., Brown, M. A., Bluhm, H., Krisch, M. J., Salmeron, M., Jungwirth, P., and Hemminger,
670 J. C.: Ion partitioning at the liquid/vapor interface of a multicomponent alkali halide solution: a
671 model for aqueous sea salt aerosols, *J. Phys. Chem. A*, 112, 12378–12384, 2008.

672 Glasow, R. V., Sander, R., Bott, A., and Crutzen, P. J.: Modeling halogen chemistry in the marine
673 boundary layer 1. Cloud-free MBL, *J. Geophys. Res.-Atmos.*, 107, 9-1–9-16, 2002.

674 Goodsite, M. E., Plane, J. M. C., and Skov, H.: A theoretical study of the oxidation of HgO to
675 HgBr₂ in the troposphere, *Environ. Sci. Technol.*, 38, 1772–1776, 2004.

676 Goodsite, M. E., Plane, J. M. C., and Skov, H.: Erratum: A theoretical study of the oxidation of
677 HgO to HgBr₂ in the troposphere, (*Environ. Sci. Technol.* (2004) 38:6 (1772–1776) doi:
678 10.1021/es034680s), *Environ. Sci. Technol.*, 46, 5262, doi: 10.1021/es301201c, 2012.

679 Guha, S. and Francisco, J. S.: An ab initio study of the pathways for the reaction between CH₃O₂
680 and BrO radicals, *J. Chem. Phys.*, 118, 1779–1793, doi:10.1063/1.1531099, 2003.

681 Gustin, M. S., Huang, J., Miller, M. B., Peterson, C., Jaffe, D. A., Ambrose, J., Finley, B. D.,
682 Lyman, S. N., Call, K., Talbot, R., Feddersen, D., Mao, H. and Lindberg, S. E.: Do we understand
683 what the mercury speciation instruments are actually measuring? Results of RAMIX,
684 *Environmental Science and Technology*, 47(13), 7295–7306, 2013.

685 Gustin, M. S., Amos, H. M., Huang, J., Miller, M. B., and Heidecorn, K.: Measuring and modeling
686 mercury in the atmosphere: a critical review, *Atmos. Chem. Phys.*, 15, 5697–5713, doi:
687 10.5194/acp-15-5697-2015, 2015.

688 Hall, B.: The gas phase oxidation of elemental mercury by ozone, *Water Air Soil Poll.*, 80, 301–
689 315, 1995.

690 Hanna, S. R.: Air quality model evaluation and uncertainty, *JAPCA J. Air Waste Ma.*, 38, 406–
691 412, doi: 10.1080/08940630.1988.10466390, 1988.

692 Hanna, S. R., Strimaitis, D. G., and Chang, J. C.: Hazard response modeling uncertainty (a
693 quantitative method), vol. I: User's guide for software for evaluating hazardous gas dispersion
694 models; vol. II: Evaluation of commonly-used hazardous gas dispersion models; vol. III:
695 Components of uncertainty in hazardous gas dispersion models, Sigma Research Corporation,
696 Westford, USA, 1991.

697 Hanna, S. R., Chang, J. C., and Strimaitis, D. G.: Hazardous gas model evaluation with field
698 observations, *Atmos. Environ. A-Gen.*, 27, 2265–2285, doi: 10.1016/0960-1686(93)90397-H,
699 1993.

700 Hedgecock, I. M. and Pirrone, N.: Chasing quicksilver: modeling the atmospheric lifetime of Hg⁰
701 (g) in the marine boundary layer at various latitudes, *Environ. Sci. Technol.*, 38, 69–76, 2004.

702 Hedgecock, I. M. and Pirrone, N.: Modelling chemical and physical processes of Hg compounds
703 in the marine boundary layer, *Dyn. Mercury Pollut. Reg. Glob. Scales Atmospheric Process. Hum.*
704 *Expo. World*, 2005.

705 Hedgecock, I. M., Pirrone, N., Sprovieri, F., and Pesenti, E.: Reactive gaseous mercury in the
706 marine boundary layer: modelling and experimental evidence of its formation in the Mediterranean
707 region, *Atmos. Environ.*, 37, S41–S49, 2003.

708 Hess, M., Krieger, U. K., Marcolli, C., Huthwelker, T., Ammann, M., Lanford, W. A., and Peter,
709 T.: Bromine enrichment in the near-surface region of Br-doped NaCl single crystals diagnosed by
710 rutherford backscattering spectrometry, *J. Phys. Chem. A*, 111, 4312–4321, 2007.

711 Holmes, C. D., Jacob, D. J., and Yang, X.: Global lifetime of elemental mercury against oxidation
712 by atomic bromine in the free troposphere, *Geophys. Res. Lett.*, 33, L20808, doi:
713 10.1029/2006GL027176, 2006.

714 Holmes, C. D., Jacob, D. J., Mason, R. P., and Jaffe, D. A.: Sources and deposition of reactive
715 gaseous mercury in the marine atmosphere, *Atmos. Environ.*, 43, 2278–2285, 2009.

716 Holmes, C. D., Jacob, D. J., Corbitt, E. S., Mao, J., Yang, X., Talbot, R., and Slemr, F.: Global
717 atmospheric model for mercury including oxidation by bromine atoms, *Atmos. Chem. Phys.*, 10,
718 12037–12057, doi:10.5194/acp-10-12037-2010, 2010.

719 Huang, J., Miller, M. B., Weiss-Penzias, P. and Gustin, M. S.: Comparison of gaseous oxidized
720 Hg measured by KCl-coated denuders, and nylon and cation exchange membranes, *Environmental*
721 *Science and Technology*, 47(13), 7307–7316, 2013.

722 Jaffe, D. A., Lyman, S., Amos, H. M., Gustin, M. S., Huang, J., Selin, N. E., Levin, L., ter Schure,
723 A., Mason, R. P., Talbot, R., Rutter, A., Finley, B., Jaeglé, L., Shah, V., McClure, C., Ambrose,
724 J., Gratz, L., Lindberg, S., Weiss-Penzias, P., Sheu, G.-R., Feddersen, D., Horvat, M., Dastoor, A.,
725 Hynes, A. J., Mao, H., Sonke, J. E., Slemr, F., Fisher, J. A., Ebinghaus, R., Zhang, Y., and Edwards,

- 726 G.: Progress on understanding atmospheric mercury hampered by uncertain measurements,
727 *Environ. Sci. Technol.*, 48, 7204–7206, doi: 10.1021/es5026432, 2014.
- 728 Kim, P.-R., Han, Y.-J., Holsen, T. M., and Yi, S.-M.: Atmospheric particulate mercury:
729 concentrations and size distributions, *Atmos. Environ.*, 61, 94–102, 2012.
- 730 Kim, S. Y., Talbot, R., Mao, H., Blake, D. R., Huey, G., and Weinheimer, A. J.: Chemical
731 transformations of Hg during Arctic mercury depletion events sampled from the NASA DC-8,
732 *Atmos. Chem. Phys. Discuss.*, 10, 10077–10112, doi: 10.5194/acpd-10-10077-2010, 2010.
- 733 Kutsher, J., Haikin, N., Sharon, A., and Heifetz, E.: On the formation of an elevated nocturnal
734 inversion layer in the presence of a low-level jet: a case study, *Bound.-Lay. Meteorol.*, 144, 441–
735 449, doi:10.1007/s10546-012-9720-y, 2012.
- 736 Laskin, A., Moffet, R. C., Gilles, M. K., Fast, J. D., Zaveri, R. A., Wang, B., Nigge, P., and
737 Shutthanandan, J.: Tropospheric chemistry of internally mixed sea salt and organic particles:
738 surprising reactivity of NaCl with weak organic acids, *J. Geophys. Res.-Atmos.*, 117, D15302, doi:
739 10.1029/2012JD017743, 2012.
- 740 Laurier, F. and Mason, R.: Mercury concentration and speciation in the coastal and open ocean
741 boundary layer, *J. Geophys. Res.-Atmos.*, 112, D06302, doi: 10.1029/2006JD007320, 2007.
- 742 Laurier, F. J. G., Mason, R. P., Whalin, L., and Kato, S.: Reactive gaseous mercury formation in
743 the North Pacific Ocean’s marine boundary layer: a potential role of halogen chemistry, *J. Geophys.*
744 *Res.-Atmos.*, 108, ACH3-1—ACH3-12, doi: 10.1029/2003JD003625, 2003.
- 745 Lewis, E. R. and Schwartz, S. E.: Comment on “Size distribution of sea-salt emissions as a function
746 of relative humidity,” *Atmos. Environ.*, 40, 588–590, doi: 10.1016/j.atmosenv.2005.08.043, 2006.
- 747 Lin, C.-J. and Pehkonen, S. O.: Aqueous phase reactions of mercury with free radicals and chlorine:
748 implications for atmospheric mercury chemistry, *Chemosphere*, 38, 1253–1263, 1999.
- 749 Lin, C.-J., Pongprueksa, P., Lindberg, S. E., Pehkonen, S. O., Byun, D., and Jang, C.: Scientific
750 uncertainties in atmospheric mercury models I: Model science evaluation, *Atmos. Environ.*, 40,
751 2911–2928, 2006.
- 752 Lindberg, S. E., Brooks, S., Lin, C.-J., Scott, K. J., Landis, M. S., Stevens, R. K., Goodsite, M.,
753 and Richter, A.: Dynamic oxidation of gaseous mercury in the arctic troposphere at polar sunrise,
754 *Environ. Sci. Technol.*, 36, 1245–1256, 2002.
- 755 Madronich, S.: UV radiation in the natural and perturbed atmosphere, in: *Environmental Effects*
756 *of UV*, CRC Press, Boca Raton, FL, USA, available at:
757 <http://opensky.library.ucar.edu/collections/OSGC-000-000-020-698> (last access: 16 April 2015),
758 1993.
- 759 Mao, H. and Talbot, R.: O₃ and CO in New England: temporal variations and relationships, *J.*
760 *Geophys. Res.-Atmos.*, 109, D21304, doi: 10.1029/2004JD004913, 2004.

761 Mao, H., Talbot, R. W., Sigler, J. M., Sive, B. C., and Hegarty, J. D.: Seasonal and diurnal
762 variations of Hg over New England, *Atmos. Chem. Phys.*, 8, 1403–1421, doi: 10.5194/acp-8-1403-
763 2008, 2008.

764 Mao, H., Talbot, R., Hegarty, J., and Koerner, J.: Speciated mercury at marine, coastal, and inland
765 sites in New England – Part 2: Relationships with atmospheric physical parameters, *Atmos. Chem.*
766 *Phys.*, 12, 4181–4206, doi: 10.5194/acp-12-4181-2012, 2012.

767 Mason, R. P., Kim, E.-H., Cornwell, J., and Heyes, D.: An examination of the factors influencing
768 the flux of mercury, methylmercury and other constituents from estuarine sediment, *Mar. Chem.*,
769 102, 96–110, 2006.

770 Miller, C. L., Mason, R. P., Gilmour, C. C., and Heyes, A.: Influence of dissolved organic matter
771 on the complexation of mercury under sulfidic conditions, *Environ. Toxicol. Chem.*, 26, 624–633,
772 2007.

773 Moldanová, J. and Ljungström, E.: Sea-salt aerosol chemistry in coastal areas: a model study, *J.*
774 *Geophys. Res.-Atmos.*, 106, 1271–1296, doi: 10.1029/2000JD900462, 2001.

775 Obrist, D., Tas, E., Peleg, M., Matveev, V., Faïn, X., Asaf, D., and Luria, M.: Bromine-induced
776 oxidation of mercury in the mid-latitude atmosphere, *Nat. Geosci.*, 4, 22–26, 2011.

777 Pal, B. and Ariya, P. A.: Gas-phase HO-initiated reactions of elemental mercury: kinetics, product
778 studies, and atmospheric implications, *Environ. Sci. Technol.*, 38, 5555–5566, 2004a.

779 Pal, B. and Ariya, P. A.: Studies of ozone initiated reactions of gaseous mercury: kinetics, product
780 studies, and atmospheric implications, *Phys. Chem. Chem. Phys.*, 6, 572–579, 2004b.

781 Pillai, P. S. and Moorthy, K. K.: Aerosol mass-size distributions at a tropical coastal environment:
782 response to mesoscale and synoptic processes, *Atmos. Environ.*, 35, 4099–4112, doi:
783 10.1016/S1352-2310(01)00211-4, 2001.

784 Poissant, L., Pilote, M., Beauvais, C., Constant, P. and Zhang, H. H.: A year of continuous
785 measurements of three atmospheric mercury species (GEM, RGM and Hgp) in southern Québec,
786 Canada, *Atmospheric Environment*, 39(7), 1275–1287, 2005.

787 Raofie, F. and Ariya, P. A.: Product study of the gas-phase BrO-initiated oxidation of Hg⁰:
788 Evidence for stable Hg¹⁺ compounds, *Environ. Sci. Technol.*, 38, 4319–4326, 2004.

789 Rolfhus, K. R., Sakamoto, H. E., Cleckner, L. B., Stoor, R. W., Babiarz, C. L., Back, R. C.,
790 Manolopoulos, H., and Hurley, J. P.: Distribution and fluxes of total and methylmercury in Lake
791 Superior, *Environ. Sci. Technol.*, 37, 865–872, 2003.

792 Rutter, A. P. and Schauer, J. J.: The impact of aerosol composition on the particle to gas
793 partitioning of reactive mercury, *Environ. Sci. Technol.*, 41, 3934–3939, doi: 10.1021/es062439i,
794 2007.

- 795 Rutter, A. P., Shakya, K. M., Lehr, R., Schauer, J. J., and Griffin, R. J.: Oxidation of gaseous
796 elemental mercury in the presence of secondary organic aerosols, *Atmos. Environ.*, 59, 86–92,
797 2012.
- 798 Saiz-Lopez, A. and von Glasow, R.: Reactive halogen chemistry in the troposphere, *Chem. Soc.*
799 *Rev.*, 41, 6448–6472, doi: 10.1039/C2CS35208G, 2012.
- 800 Saiz-Lopez, A., Shillito, J. A., Coe, H., and Plane, J. M. C.: Measurements and modelling of I₂,
801 IO, OIO, BrO and NO₃ in the mid-latitude marine boundary layer, *Atmos. Chem. Phys.*, 6, 1513–
802 1528, doi:10.5194/acp-6-1513-2006, 2006.
- 803 Sander, R., Keene, W. C., Pszenny, A. A. P., Arimoto, R., Ayers, G. P., Baboukas, E., Caine, J.
804 M., Crutzen, P. J., Duce, R. A., Hönninger, G., Huebert, B. J., Maenhaut, W., Mihalopoulos, N.,
805 Turekian, V. C., and Van Dingenen, R.: Inorganic bromine in the marine boundary layer: a critical
806 review, *Atmos. Chem. Phys.*, 3, 1301–1336, doi:10.5194/acp-3-1301-2003, 2003.
- 807 Sander, S. P., Abbatt, J., Barker, J. R., Burkholder, J. B., Friedl, R. R., Golden, D. M., Huie, R. E.,
808 Kolb, C. E., Kurylo, M. J., Moortgat, G. K., Orkin, V. L., and Wine, P. H.: Chemical Kinetics and
809 Photochemical Data for Use in Atmospheric Studies, Evaluation No. 17, JPL Publication 10-6, Jet
810 Propulsion Laboratory, Pasadena, available at: <http://jpldataeval.jpl.nasa.gov>, 2011.
- 811 Sandu, A. and Sander, R.: Technical note: Simulating chemical systems in Fortran90 and Matlab
812 with the Kinetic PreProcessor KPP-2.1, *Atmos. Chem. Phys.*, 6, 187–195, doi: 10.5194/acp-6-187-
813 2006, 2006.
- 814 Schroeder, W. H. and Munthe, J.: Atmospheric mercury – an overview, *Atmos. Environ.*, 32, 809–
815 822, 1998.
- 816 Schwartz, S. E.: Mass-transport considerations pertinent to aqueous phase reactions of gases in
817 liquid-water clouds, in: *Chemistry of Multiphase Atmospheric Systems*, edited by: Jaeschke, D.
818 W., Springer, Berlin, Heidelberg, 415–471, available at: [http://link.springer.com/
819 chapter/10.1007/978-3-642-70627-1_16](http://link.springer.com/chapter/10.1007/978-3-642-70627-1_16) (last access: 17 April 2015), 1986.
- 820 Selin, N. E., Jacob, D. J., Park, R. J., Yantosca, R. M., Strode, S., Jaeglé, L., and Jaffe, D.:
821 Chemical cycling and deposition of atmospheric mercury: global constraints from observations, *J.*
822 *Geophys. Res.-Atmos.*, 112, D02308, doi: 10.1029/2006JD007450, 2007.
- 823 Seigneur, C., Wrobel, J. and Constantinou, E.: A chemical kinetic mechanism for atmospheric
824 inorganic mercury, *Environmental Science and Technology*, 28(9), 1589–1597, 1994.
- 825 Shon, Z.-H., Kim, K.-H., Kim, M.-Y., and Lee, M.: Modeling study of reactive gaseous mercury
826 in the urban air, *Atmos. Environ.*, 39, 749–761, 2005.
- 827 Sigler, J. M., Mao, H., and Talbot, R.: Gaseous elemental and reactive mercury in Southern New
828 Hampshire, *Atmos. Chem. Phys.*, 9, 1929–1942, doi:10.5194/acp-9-1929-2009, 2009.

- 829 Sillman, S., Marsik, F. J., Al-Wali, K. I., Keeler, G. J., and Landis, M. S.: Reactive mercury in the
830 troposphere: model formation and results for Florida, the northeastern United States, and the
831 Atlantic Ocean, *J. Geophys. Res.-Atmos.*, 112, D23305, doi: 10.1029/2006JD008227, 2007.
- 832 Simpson, W. R., von Glasow, R., Riedel, K., Anderson, P., Ariya, P., Bottenheim, J., Burrows, J.,
833 Carpenter, L. J., Frieß, U., Goodsite, M. E., Heard, D., Hutterli, M., Jacobi, H.-W., Kaleschke, L.,
834 Neff, B., Plane, J., Platt, U., Richter, A., Roscoe, H., Sander, R., Shepson, P., Sodeau, J., Steffen,
835 A., Wagner, T., and Wolff, E.: Halogens and their role in polar boundary layer ozone depletion,
836 *Atmos. Chem. Phys.*, 7, 4375–4418, doi:10.5194/acp-7-4375-2007, 2007.
- 837 Simpson, W. R., Brown, S. S., Saiz-Lopez, A., Thornton, J. A., and von Glasow, R.: Tropospheric
838 halogen chemistry: sources, cycling, and impacts, *Chem. Rev.*, 115, 4035–4062, doi:
839 10.1021/cr5006638, 2015.
- 840 Snider, G., Raofie, F., and Ariya, P. A.: Effects of relative humidity and CO (g) on the O₃-initiated
841 oxidation reaction of HgO (g): kinetic and product studies, *Phys. Chem. Chem. Phys.*, 10, 5616–
842 5623, 2008.
- 843 Soerensen, A. L., Sunderland, E. M., Holmes, C. D., Jacob, D. J., Yantosca, R. M., Skov, H.,
844 Christensen, J. H., Strode, S. A., and Mason, R. P.: An improved global model for air–sea exchange
845 of mercury: high concentrations over the North Atlantic, *Environ. Sci. Technol.*, 44, 8574–8580,
846 2010.
- 847 Steffen, A., Douglas, T., Amyot, M., Ariya, P., Aspö, K., Berg, T., Bottenheim, J., Brooks, S.,
848 Cobbett, F., Dastoor, A., Dommergue, A., Ebinghaus, R., Ferrari, C., Gardfeldt, K., Goodsite, M.
849 E., Lean, D., Poulain, A. J., Scherz, C., Skov, H., Sommar, J., and Temme, C.: A synthesis of
850 atmospheric mercury depletion event chemistry in the atmosphere and snow, *Atmos. Chem. Phys.*,
851 8, 1445–1482, doi:10.5194/acp-8-1445-2008, 2008.
- 852 Subir, M., Ariya, P. A., and Dastoor, A. P.: A review of uncertainties in atmospheric modeling of
853 mercury chemistry I. Uncertainties in existing kinetic parameters – fundamental limitations and
854 the importance of heterogeneous chemistry, *Atmos. Environ.*, 45, 5664–5676, 2011.
- 855 Talbot, R., Mao, H., and Sive, B.: Diurnal characteristics of surface level O₃ and other important
856 trace gases in New England, *J. Geophys. Res.*, 110, D09307, doi: 10.1029/2004JD005449, 2005.
- 857 Tang, I. N., Tridico, A. C., and Fung, K. H.: Thermodynamic and optical properties of sea salt
858 aerosols, *J. Geophys. Res.-Atmos.*, 102, 23269–23275, 1997.
- 859 Tokos, J. J. S., Hall, B., Calhoun, J. A., and Prestbo, E. M.: Homogeneous gas-phase reaction of
860 HgO with H₂O₂, O₃, CH₃I, and (CH₃)₂S: implications for atmospheric Hg cycling, *Atmos. Environ.*,
861 32, 823–827, 1998.
- 862 Toyota, K., McConnell, J. C., Staebler, R. M., and Dastoor, A. P.: Air–snowpack exchange of
863 bromine, ozone and mercury in the springtime Arctic simulated by the 1-D model PHANTAS–
864 Part 1: In-snow bromine activation and its impact on ozone, *Atmos. Chem. Phys.*, 14, 4101–4133,
865 doi:10.5194/acp-14-4101-2014, 2014.

- 866 Verwer, J. G., Spee, E. J., Blom, J. G., and Hundsdorfer, W.: Second-order Rosenbrock method
867 applied to photochemical dispersion problems, *SIAM J. Sci. Comput.*, 20, 1456–1480, 1999.
- 868 Wang, F., Saiz-Lopez, A., Mahajan, A. S., Gómez Martín, J. C., Armstrong, D., Lemes, M., Hay,
869 T., and Prados-Roman, C.: Enhanced production of oxidized mercury over the tropical Pacific
870 Ocean: a key missing oxidation pathway, *Atmos. Chem. Phys.*, 14, 1323–1335, doi:10.5194/acp-
871 14-1323-2014, 2014.
- 872 Weiss-Penzias, P., Jaffe, D. A., McClintick, A., Prestbo, E. M. and Landis, M. S.: Gaseous
873 elemental mercury in the marine boundary layer: evidence for rapid removal in anthropogenic
874 pollution, *Environ. Sci. Technol.*, 37(17), 3755–3763, 2003.
- 875 Xie, Z.-Q., Sander, R., Pöschl, U., and Slemr, F.: Simulation of atmospheric mercury depletion
876 events (AMDEs) during polar springtime using the MECCA box model, *Atmos. Chem. Phys.*, 8,
877 7165–7180, doi: 10.5194/acp-8-7165-2008, 2008.
- 878 Zhang, L., Wright, L. P., and Blanchard, P.: A review of current knowledge concerning dry
879 deposition of atmospheric mercury, *Atmos. Environ.*, 43, 5853–5864, 2009.
- 880 Zhang, L., Blanchard, P., Gay, D. A., Prestbo, E. M., Risch, M. R., Johnson, D., Narayan, J.,
881 Zsolway, R., Holsen, T. M., Miller, E. K., Castro, M. S., Graydon, J. A., Louis, V. L. S., and
882 Dalziel, J.: Estimation of speciated and total mercury dry deposition at monitoring locations in
883 eastern and central North America, *Atmos. Chem. Phys.*, 12, 4327–4340, 2012.

884 Table 1. Gas phase Hg reactions in the box model

No.	REACTIONS	KINETIC (cm ³ molecule ⁻¹ s ⁻¹)	REFERENCE
G1	Hg + O ₃ → HgO + O ₂	$8.43 \times 10^{-17} e^{-1407/T}$	Snider et al., 2008
G2	Hg + OH {+O ₂ } → HgO + HO ₂	$3.55 \times 10^{-14} e^{294/T}$	Pal and Ariya, 2004
G3	Hg + H ₂ O ₂ → Hg(OH) ₂	8.5×10^{-19}	Tokos et al., 1998
G4	Hg + Cl → HgCl	$6.4 \times 10^{-13} e^{(680 \times (1/T - 1/298))}$	Donohoue et al., 2005
G5	Hg + Cl ₂ → HgCl ₂	2.6×10^{-18}	Ariya et al., 2002
G6	Hg + Br → HgBr	$3.7 \times 10^{-13} (T/298)^{-2.76}$	Goodsite et al., 2004, 2012
G7	Hg + BrO → HgBrO	1.8×10^{-14}	Raofie and Ariya, 2004
G8	Hg + I → HgI	$4.0 \times 10^{-13} (T/298)^{-2.38}$	Goodsite et al., 2004
G9	HgI → Hg + I	$3.0 \times 10^9 e^{-3742/T}$	Goodsite et al., 2004
G10	HgBr → Hg + Br	$1.6 \times 10^{-9} e^{-7801/T} \times [M]$	Dibble et al., 2012
G11	HgBr + Br → Hg + Br ₂	3.89×10^{-11}	Balabanov et al., 2005
G12	HgBr + Br → HgBr + Br	3.97×10^{-11}	Balabanov et al., 2005
G13	HgBr + Br → HgBr ₂	2.98×10^{-11}	Balabanov et al., 2005
G14	ClO + HgCl → ClHgOCl	5.0×10^{-11}	Dibble et al., 2012
G15	ClO + HgBr → BrHgOCl	5.0×10^{-11}	Dibble et al., 2012
G16	BrO + HgCl → BrHgOCl	1.09×10^{-10}	Dibble et al., 2012 ¹
G17	BrO + HgBr → BrHgOBr	1.09×10^{-10}	Dibble et al., 2012; Wang et al., 2014
G18	NO ₂ + HgCl → ClHgNO ₂	8.6×10^{-11}	Dibble et al., 2012 ¹
G19	NO ₂ + HgBr → BrHgNO ₂	8.6×10^{-11}	Dibble et al., 2012; Wang et al., 2014
G20	HO ₂ + HgCl → ClHgOOH	8.2×10^{-11}	Dibble et al., 2012 ¹
G21	HO ₂ + HgBr → BrHgOOH	8.2×10^{-11}	Dibble et al., 2012; Wang et al., 2014
G22	OH + HgCl → ClHgOH	6.33×10^{-11}	Dibble et al., 2012 ¹
G23	OH + HgBr → BrHgOH	6.33×10^{-11}	Dibble et al., 2012; Wang et al., 2014
G24	IO + HgBr → BrHgOI	4.9×10^{-11}	Wang et al., 2014

885 ¹ The kinetic data of these HgCl reactions were not included in Dibble et al., 2012, they were assumed as the same
886 kinetic as the HgBr reactions, which were calculated by Wang et al. (2014).
887

888 Table 2. Box model input and simulated variables.

Parameter	Appledore Island (AI)	Thompson Farm (TF)	Pack Monadnock (PM)
Observed¹			
RH, relative humidity	76.9±5.4	69.9±19.5	69.0±13.1
Temperature, °C	19.1±1.7	21.3±4.3	18.5±3.3
[GEM], ppqv	133.9±3.3	138.4±12.8	149.6±3.2
[O ₃], ppbv	37.4±8.8	32.7±15.7	45.0±4.2
[NO], pptv	154.5 ²	232.4±364.1	85.3±35.8
[CO], ppbv	169.6±13.9	156.2±10.8	120.2±7.2
Simulated³			
[Br], ppqv	28.50	0.20	0.18
[OH], ppqv	100.7	75.8	73.5
Other⁴			
v_d , cm s ⁻¹ , dry deposition velocity	GEM – 0.0045	GEM – 0.07	GEM – 0.08
	GOM – 0.5	GOM – 1.2	GOM – 2.0
	PBM – 0.5	PBM – 0.15	PBM – 0.25
H, M atm ⁻¹ , Henry's constants	HgO – 3.2×10^9	HgO – 3.2×10^9	HgO – 3.2×10^9
	Hg(OH) ₂ – 1.2×10^7	Hg(OH) ₂ – 1.2×10^7	Hg(OH) ₂ – 1.2×10^7
	Other GOM – 2.7×10^9	Other GOM – 2.7×10^9	Other GOM – 2.7×10^9
L, m ³ _{water} m ⁻³ _{air} , liquid water content	5×10^{-11}	2.0×10^{-11}	1.25×10^{-11}
D _g , m ² s ⁻¹ , diffusion coefficient	1×10^{-5}	1×10^{-5}	1×10^{-5}
Z, m, boundary layer height	500	200 – 1120 ⁵	100
r_{dry} , μm, dry aerosol radius	3.5	0.3	0.07

889 ¹ Observed 24-h mean values for all studied cases at these sites.890 ² Missing NO measurements at AI, use 154.5 ppqv for initial values.891 ³ Simulated 24-h mean values for all studied days at these sites.892 ⁴ Reference: Baumgardner et al., 2000; Kim et al., 2012; Mao and Talbot, 2004; Moldanová and Ljungström, 2001; Pillai and Moorthy, 2001; Shon et al., 2005; Zhang et al., 2009, 2012.893 ⁵ TF boundary layer height changed at each hour, the averaged diurnal cycle was obtained from Research Data Archive at the National Center for Atmospheric Research, <http://rda.ucar.edu/>.

894

895

896

897

Table 3. Sensitivity scenarios with varying physical and chemical parameters. The superscript D represents daytime and N nighttime. Downward arrows stand for decreases and upward arrows increases. T stands for the temperature diurnal cycle in the base scenario, and T+10K or T-10K represents 10K higher temperature or 10K lower temperature throughout the day respectively.

Scenario No.	photolysis	Gas-droplet partitioning		Rate Coefficients ($\text{cm}^3 \text{ molec}^{-1} \text{ s}^{-1}$)			Temp.	Results	
		Include	Liquid water content ($\text{m}^3_{\text{water}} \text{m}^{-3}_{\text{air}}$)	GEM+O ₃ (298K)	GEM+OH (298K)	GEM+Br (298K)		GOM	PBM
Base Scenario									
0	Yes	Yes	5.0E-11	7.5E-19 ¹	9.5E-14 ²	3.7E-13 ³	T	--	--
Photochemistry									
1	No	Yes	5.0E-11	7.5E-19	9.5E-14	3.7E-13	T	↓ 3%-92% ^D	↓ 2-100% ^D
Gas-particle partitioning									
2	Yes	No	--	7.5E-19	9.5E-14	3.7E-13	T	↑ ~280%	↓ 100%
Liquid water content									
3	Yes	Yes	3.0E-12	7.5E-19	9.5E-14	3.7E-13	T	↑ ~200%	↓ 80%
4	Yes	Yes	3.0E-10	7.5E-19	9.5E-14	3.7E-13	T	↓ 80%	↑ 50%
Reactions									
5	Yes	Yes	5.0E-11	3.0E-20 ⁴	9.5E-14	3.7E-13	T	↓ 15% ^D ↓ 85% ^N	↓ 49% ^N
6	Yes	Yes	5.0E-11	--	9.5E-14	3.7E-13	T	↓ 16% ^D ↓ 88% ^N	↓ 51% ^N
7	Yes	Yes	5.0E-11	7.5E-19	--	3.7E-13	T	↓ 10% ^D	Negligible
8	Yes	Yes	5.0E-11	7.5E-19	9.5E-14	--	T	↓ 48% ^D	↓ 60% ^D
9	Yes	Yes	5.0E-11	7.5E-19	9.5E-14	3.2E-12 ⁵	T	↑ 250% ^D	↑ 300%
Temperature									
10	Yes	Yes	5.0E-11	7.5E-19	9.5E-14	3.7E-13	T+10K	↓ 9% ^D ↑ 13% ^N	↓ 9% ^D ↑ 54% ^N
11	Yes	Yes	5.0E-11	7.5E-19	9.5E-14	3.7E-13	T-10K	↑ 9% ^D ↓ 11% ^N	↑ 8% ^D ↓ 28% ^N

¹ Snider et al., 2008; ² Pal and Ariya, 2004; ³ Goodsite et al., 2004, 2012; ⁴ Hall, 1995; ⁵ Ariya et al., 2002.

Table 4. Possible pathways of BrO + CH₃O₂ reaction

NO.	Reactions	Kinetics (cm ³ molecule ⁻¹ s ⁻¹)	Reference
B1	$BrO(g) + CH_3O_2(g) \rightarrow CH_3O(g) + BrOO(g)$ $BrOO(g) \rightarrow Br(g) + O_2(g)$	1.4×10^{-12} Fast	Aranda et al., 1997; Atkinson et al., 2008
B2	$BrO(g) + CH_3O_2(g) \rightarrow CH_2O_2(g) + HOBr(g)$	4.3×10^{-12}	Aranda et al., 1997; Atkinson et al., 2008
B3	$BrO(g) + CH_3O_2(g) \rightarrow CH_3OBr(g) + O_2(g)$?	Aranda et al., 1997
B4	$BrO(g) + CH_3O_2(g) \rightarrow CH_3OOOBr(g) \rightarrow$ $CH_2O(g) + HOOBr(g)$?	Guha and Francisco, 2003

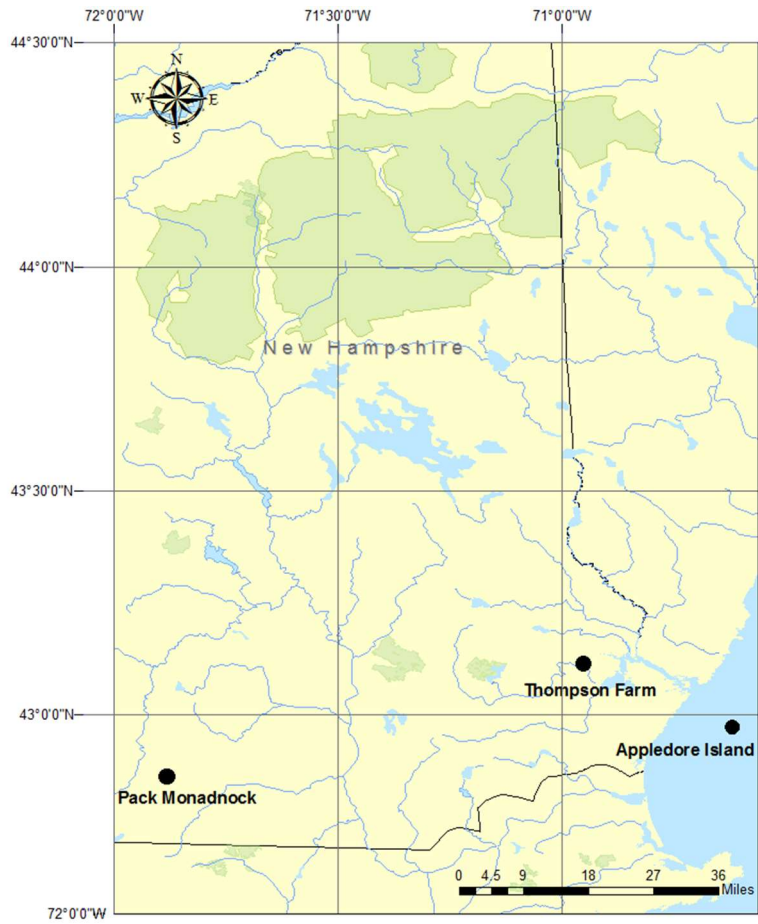


Figure 1. New Hampshire site map: Appledore Island (marine), Thompson Farm (coastal), and Pack Monadnock (inland elevated).

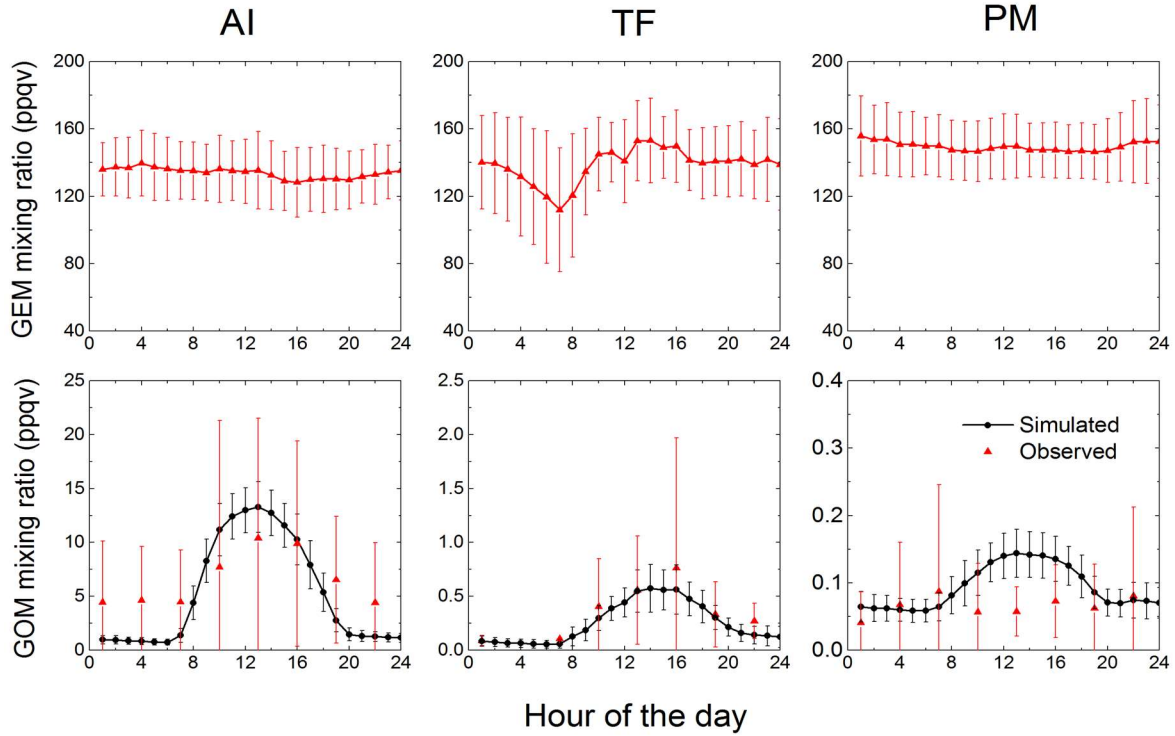


Figure 2. Average diurnal cycles of observed GEM (top panel) and simulated and observed GOM (bottom panel) averaged over the selected 50 days at Appledore Island (AI), 12 days at Thompson Farm (TF), and 21 days at Pack Monadnock (PM) from summers of 2007, 2008, and 2010. The error bars represent standard deviation.

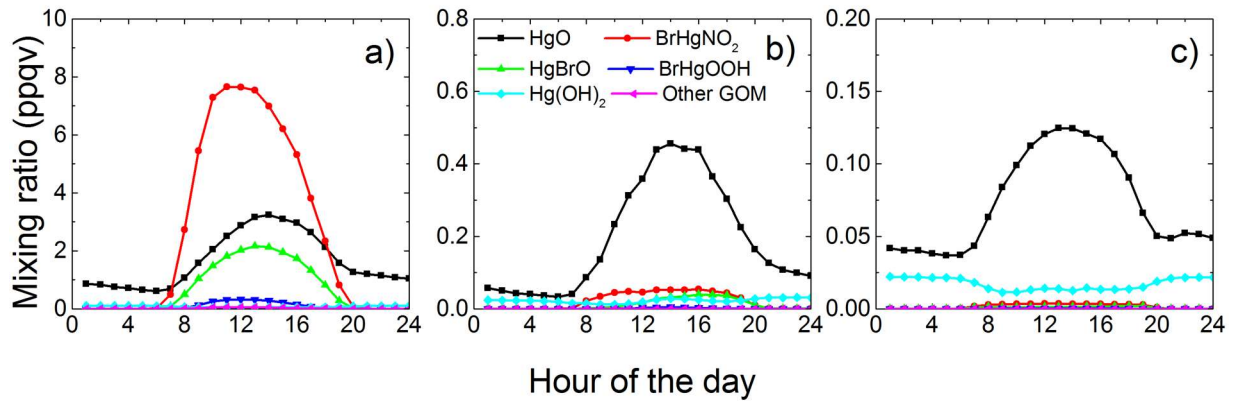


Figure 3. Simulated average diurnal cycles of GOM speciation at AI (a), TF (b), and PM (c).

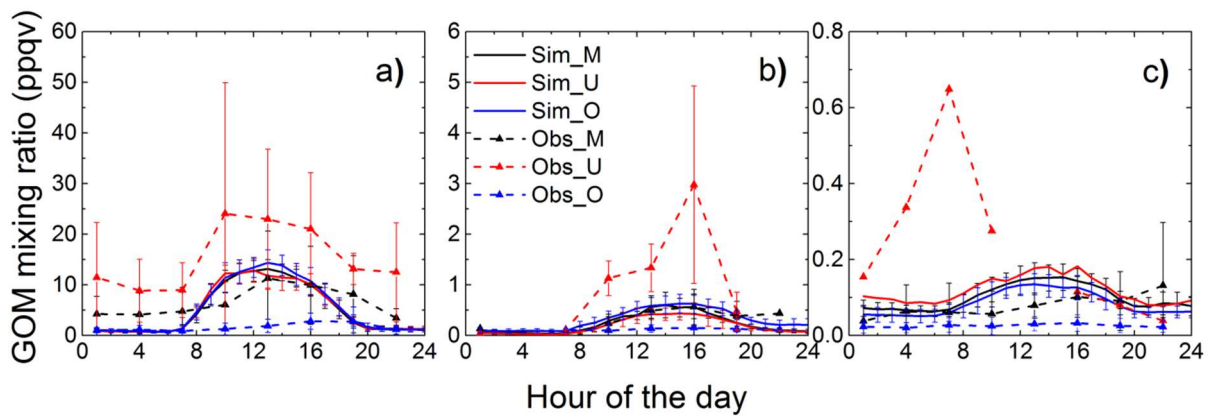


Figure 4. Observed (dash line with scatters) and simulated (solid line) average diurnal cycles of GOM for the matching (black, “Sim_M” and “Obs_M”), under-estimation (red, “Sim_U” and “Obs_U”), and over-estimation cases (blue, “Sim_O” and “Obs_O”) at AI (a), TF (b), and PM (c). The bars represent the standard deviations at each hour for those specific days.

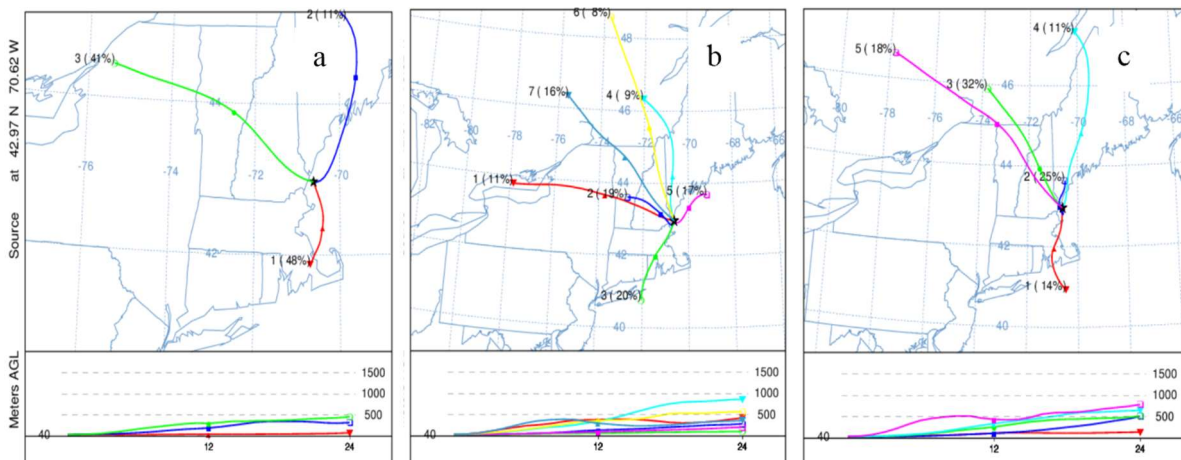


Figure 5. Clustered 24-hours back trajectories of air masses in (a) over-estimation cases, (b) matching cases, and (c) under-estimation cases at AI.

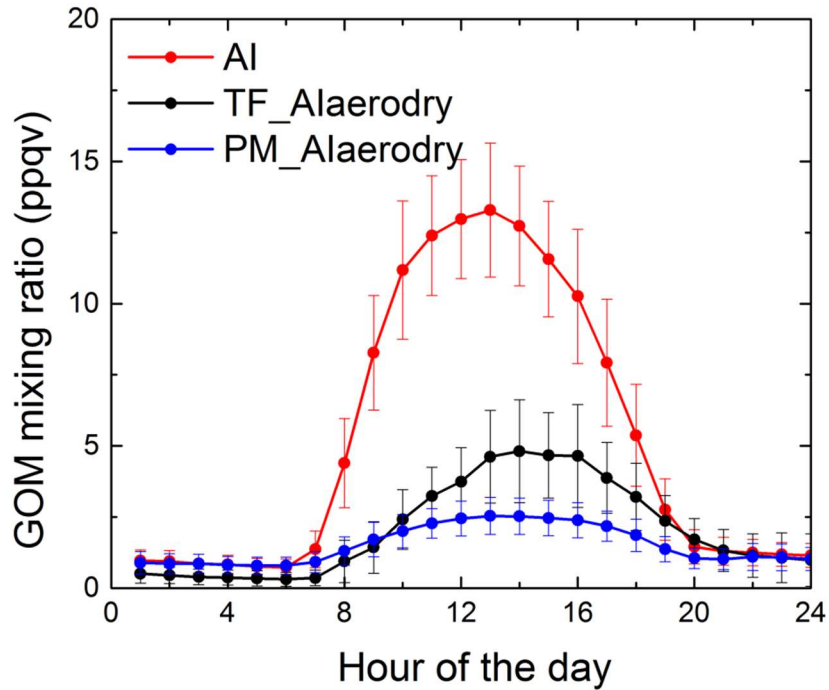


Figure 6. Simulated averaged diurnal cycles of GOM at AI (red), at TF (black) using AI dry deposition and gas-aerosol partitioning parameters (“TF_Alaerodry”), and at PM (blue) using AI dry deposition and gas-to-particle partitioning parameters (“PM_Alaerodry”).

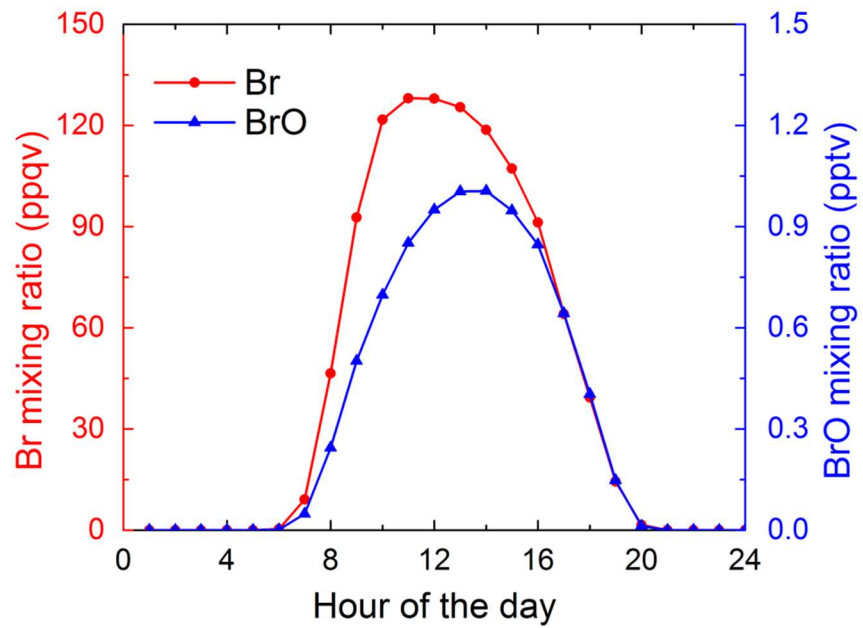


Figure 7. Simulated diurnal cycles of Br (red) and BrO (blue) of the base case.

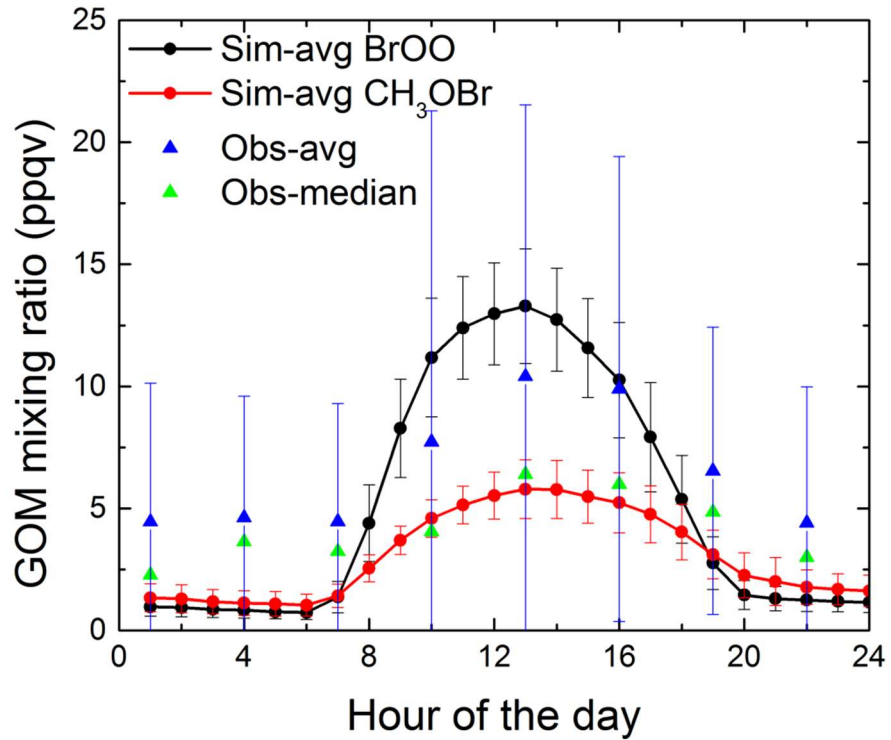


Figure8. Simulated average diurnal cycles of GOM for the base scenario (“Sim-avg BrOO”, black circle) and for the “CH₃OBr” scenario (“Sim-avg CH₃OBr”, red, circle), observed average GOM diurnal cycle (“Obs-avg”, blue, triangle scatter), and observed median GOM diurnal cycle (“Obs-median”, green, triangle scatter) of the 50 cases at AI.

Supplement:

Table S1. Aqueous phase reactions and equilibriums of Hg in the box model.

No.	REACTIONS	KINETIC (L mol ⁻¹ s ⁻¹) or EQUILIBRIUM CONSTANT	REFERENCE
A1	$\text{Hg}^0(\text{aq}) + \text{O}_3(\text{aq}) \rightarrow \text{HgO}(\text{aq}) + \text{O}_2(\text{aq})$	2.4×10^9	Munthe et al., 1992
A2	$\text{Hg}^0(\text{aq}) + \text{OH}(\text{aq}) \rightarrow \text{HgOH}(\text{aq})$	2.4×10^9	Gardfeldt et al., 2001
A3	$\text{HgOH}(\text{aq}) + \text{OH}(\text{aq}) \rightarrow \text{Hg}(\text{OH})_2(\text{aq})$	1.0×10^{10}	Nazhat and Asmus, 1973
A4	$\text{HgOH}(\text{aq}) + \text{O}_2(\text{aq}) + \text{H}_2\text{O}(\text{aq}) \rightarrow$ $\text{Hg}(\text{OH})_2(\text{aq}) + \text{H}^+ + \text{O}_2^-$	1.0×10^9	Nazhat and Asmus, 1973
A5	$\text{Hg}^0(\text{aq}) + \text{OH}(\text{aq}) \rightarrow \text{Hg}^+ + \text{OH}^-$	2.0×10^9	Lin and Pehkonen, 1997
A6	$\text{HgO}(\text{aq}) + \text{H}^+ \rightarrow \text{Hg}^{2+} + \text{OH}^-$	1.0×10^{10}	Pleijel and Munthe, 1995
A7	$\text{HOCl}(\text{aq}) + \text{Hg}^0(\text{aq}) \rightarrow \text{Hg}^{2+} + \text{Cl}^- + \text{OH}^-$	2.09×10^6	Lin and Pehkonen, 1997
A8	$\text{ClO}^- + \text{Hg}^0(\text{aq}) \rightarrow \text{Hg}^{2+} + \text{Cl}^- + \text{OH}^-$	1.99×10^6	Lin and Pehkonen, 1997
A9	$\text{HgSO}_3(\text{aq}) \rightarrow \text{Hg}^0(\text{aq}) + \text{S(VI)}$	0.6	Munthe et al., 1991
A10	$\text{Hg}(\text{OH})_2(\text{aq}) \rightarrow \text{Hg}^0(\text{aq}) + \text{products}$	3.0×10^7	Pleijel and Munthe, 1995
A11	$\text{Hg}^+ + \text{HO}_2(\text{aq}) \rightarrow \text{Hg}^0(\text{aq}) + \text{O}_2(\text{aq}) +$ H^+	1.0×10^{10}	Xie et al., 2008
A12	$\text{Hg}^{2+} + \text{HO}_2(\text{aq}) \rightarrow \text{Hg}^+ + \text{O}_2(\text{aq}) + \text{H}^+$	1.7×10^4	Pehkonen and Lin, 1998
AE1	$\text{Hg}^{2+} + \text{SO}_3^{2-} \leftrightarrow \text{HgSO}_3(\text{aq})$	2.0×10^{13}	van Loon et al., 2001
AE2	$\text{HgSO}_3(\text{aq}) + \text{SO}_3^{2-} \leftrightarrow \text{Hg}(\text{SO}_3)_2^{2-}$	1.0×10^{10}	van Loon et al., 2001
AE3	$\text{Hg}^{2+} + \text{OH}^- \leftrightarrow \text{HgOH}^+$	3.98×10^{10}	Smith and Martell, 2004
AE4	$\text{HgOH}^+ + \text{OH}^- \leftrightarrow \text{Hg}(\text{OH})_2(\text{aq})$	1.58×10^{11}	Smith and Martell, 2004
AE5	$\text{HgOH}^+ + \text{Cl}^- \leftrightarrow \text{HgOHCl}(\text{aq})$	2.7×10^7	Xiao, 1994
AE6	$\text{Hg}^{2+} + \text{Cl}^- \leftrightarrow \text{HgCl}^+$	2.0×10^7	Smith and Martell, 2004
AE7	$\text{HgCl}^+ + \text{Cl}^- \leftrightarrow \text{HgCl}_2(\text{aq})$	5.0×10^6	Smith and Martell, 2004
AE8	$\text{HgCl}_2(\text{aq}) + \text{Cl}^- \leftrightarrow \text{HgCl}_3^-$	6.7	Smith and Martell, 2004
AE9	$\text{HgCl}_3^- + \text{Cl}^- \leftrightarrow \text{HgCl}_4^{2-}$	13.0	Smith and Martell, 2004
AE10	$\text{Hg}^{2+} + \text{Br}^- \leftrightarrow \text{HgBr}^+$	1.10×10^9	Smith and Martell, 2004
AE11	$\text{HgBr}^+ + \text{Br}^- \leftrightarrow \text{HgBr}_2(\text{aq})$	2.50×10^8	Smith and Martell, 2004
AE12	$\text{HgBr}_2(\text{aq}) + \text{Br}^- \leftrightarrow \text{HgBr}_3^-$	1.50×10^2	Smith and Martell, 2004

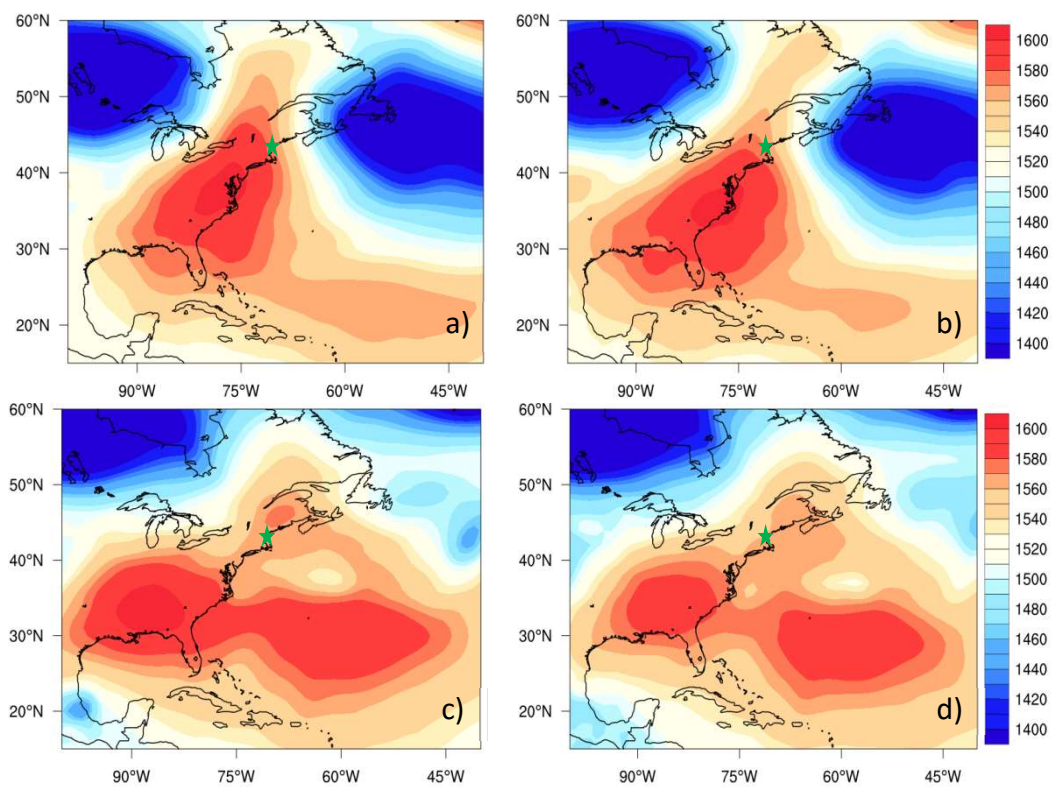


Figure S1. Geopotential height for a) 06/13/2008 08:00 EDT, b) 06/13/2008 14:00 EDT, c) 08/22/2007 14:00 EDT, and d) 08/22/2007 20:00 EDT at 850 hPa, the green star shows the location of TF site.